Complex conductivity tensor of anisotropic hydrocarbon-bearing shales and mudrocks

A. Revil (1, 2), W.F. Woodruff (1), C. Torres-Verdín (3), and M. Prasad (4)

(1) Colorado School of Mines, Department of Geophysics, Golden, 80401, CO, USA

(2) ISTerre, CNRS, UMR CNRS 5275, Université de Savoie, 73376 cedex, Le Bourget du Lac, France

(3) University of Texas at Austin, Department of Petroleum and Geosystems Engineering, Austin, TX, USA

(4) Colorado School of Mines, Department of Petroleum Engineering, Golden, 80401, CO, USA

Corresponding author: André Revil (arevil@mines.edu)

Emails:

Carlos Torres-Verdín: cverdin@austin.utexas.edu

Bill Woodruff: wfwoodruff@gmail.com

Manika Prasad: mprasad@mines.edu

Short title: Complex conductivity anisotropy

Intended for publication in Geophysics

Abstract. A model was recently introduced to describe the complex electrical conductivity and high frequency dielectric constant of isotropic clayey porous materials. That approach is generalized here to the case of anisotropic and tight hydrocarbon-bearing shales and mudrocks by introducing tensorial versions of both formation factor and tortuosity. It is shown that in-phase and quadrature conductivity tensors have common eigenvectors, but that the eigenvectors of the dielectric tensor may be different due to influence of the solid phase at high frequencies. In-phase and quadrature contributions to complex electrical conductivity depend on saturation, salinity, porosity, temperature, and cation exchange capacity (alternatively, specific surface area) of the porous material. Kerogen is likely to have a negligible contribution to the cation exchange capacity of the material because all exchangeable sites in the functional groups of organic matter may have been polymerized during diagenesis. An anisotropic experiment is performed to validate some of the properties described by the proposed model, especially to verify that the electrical anisotropy factor is the same for both in-phase and quadrature conductivities. We use two samples from the Bakken formation. Experimental data confirm the validity of the model. It is also found that the range of values for cation exchange capacity determined when implementing the new model with experimental data agree with the known range of cation exchange capacity for the Bakken shale. Measurements indicate that the bulk-space tortuosity in the direction normal to bedding plane can be higher than 100.

INTRODUCTION

Shale formations are of increasing interest in hydrocarbon exploration worldwide. They comprise a diverse set of rock types, but are generally characterized as fine-grained, low porosity and low permeability rocks, with a non-negligible clay fraction in terms of bulk petrophysical properties. Due to preferential orientation of mineral foliations and finely laminated bedding planes, shales and mudrocks are almost ubiquitously anisotropic in several of their macroscopic physical properties. The term mudrock is used to describe all fine grained shaly and non-shaly formations. It is of great interest to petrophysicists to develop new models to describe seismic and electromagnetic (EM) measurements in these anisotropic materials.

Oil-shale deposits correspond to immature, organic-rich source rocks resulting in high kerogen mass fractions due to limited burial and thermal maturation histories–effectively, they have not been heated sufficiently to release their hydrocarbons. Hence, oil shales and mudrocks are typically water-wet, single- or dual-phase fluid systems, characterized by a heterogeneous solid phase comprising both siliciclastic, carbonate, and organic components. Mudrock-oil formations involve complex multiphase fluid systems, in which the degradation of kerogen, through geochemical thermal maturation processes (i.e., catagenesis and metagenesis), has both altered the nature of the solid fraction and produced economically significant polar and non-polar, aromatic and hydrocarbon fluid fractions. Oil-shale and shale-oil deposits represent two generalized regimes in the continuum of shale thermal maturation, exhibiting measurable differences in the characteristics of both solid and fluid phases. In what follows, we refer to all these rock formations in a general manner as shales, tacitly implying that their properties are intrinsically related to the maturation history of each formation. Note however, that mudrocks is a geologically more appropriate term to use since that term denotes does not specify any lithology, rather it denotes a fine-grained rock system.

There is a growing need to better characterize the so-called "sweet spots" of tight oil-mudrock formations using an arsenal of geophysical methods with the objective to optimize hydrocarbon detection and production. Among such methods, galvanic and EM measurements can be used to determine the complex electrical conductivity of formations through borehole and cross-well imaging. What is missing is a general effective complex electrical conductivity model specific for shales and mudrocks, which includes the relative effects of porosity, water saturation, kerogen content and type, clay content and type, and a tortuosity tensor describing the anisotropy of the material (generally expected to be transversely isotropic, TI). As discussed in Revil (2013), such a model should also include the description of the high frequency permittivity of the material and possibly Maxwell-Wagner polarization. Recent developments in logging technology now allow one to resolve the macroscopic effects of anisotropy. Despite progresses on the experimental front (e.g., Weller et al., 2010), robust theoretical models describing the full effective complex conductivity tensor are still lacking (Bittar et al., 2009).

Revil and colleagues (Leroy et al., 2008; Leroy and Revil, 2009; Revil and Florsch, 2010) have recently invoked a strong role of the Stern layer (the inner portion of the electrical double layer coating the surface of mineral grains) to explain the low-frequency polarization of mixed, sandy, and clayey materials. The model of Stern layer polarization appears to be reliable to explain the dependence of complex electrical conductivity on cation exchange capacity (CEC) and specific surface area (Revil, 2012, 2013), salinity (Revil and Skold, 2011; Weller and Slater, 2012), pH (Skold et al., 2011), sorption of cations and organic molecules (Vaudelet et al., 2011a, b; Schwartz and Furman, 2012), influence of grain size (Revil et al., 2012), the relationship between surface conductivity and quadrature conductivity (Revil and Florsch, 2010; Revil, 2012), temperature (Zisser et al., 2010a), and water saturation (Revil et al., 2012; Revil, 2013). Here, we generalize this model to the case of anisotropic formations

with the intent to quantify the role played by kerogen on both surface conductivity and quadrature conductivity. Beside the contribution of the electrical double layer of non-conducting minerals, there is also a strong role played by the presence of pyrite above oil reservoirs (e.g., Veeken et al., 2009) and in the shallow subsurface associated with the biochemistry of contaminant plumes (Flores Orozco et al., 2011). Pyrite plays an active role in spectral induced polarization as long as its surface has not been oxidized. In addition, with the exception of the work by Zisser and Nover (2009) and Zisser et al. (2010b), there are a few open publications documenting and or explaining the polarization and anisotropy of tight (low-permeability) porous rocks.

THE ISOTROPIC CASE AND ITS GENERALIZATION

Ampère's law in isotropic media

Let $\omega = 2\,\pi\,f$ designate angular frequency and $f = \omega/(2\pi)$ linear frequency (in Hertz). For isotropic materials, Ampère's law is written as (e.g., Vinegar and Waxman, 1984)

$$\nabla \times \mathbf{H} = \left[\sigma_{eff} - i\omega\varepsilon_{eff}\right]\mathbf{E}, \tag{1}$$

$$\sigma_{eff} = \sigma'(\omega) + \omega\varepsilon''(\omega), \tag{2}$$

and

$$\varepsilon_{eff} = \varepsilon'(\omega) - \frac{\sigma''(\omega)}{\omega}, \tag{3}$$

where **H** and **E** denote magnetic and electrical fields, respectively, $i = \sqrt{-1}$ denotes the pure imaginary number, and σ' and σ'' (expressed in S m^{-1}) denote the real (in-phase) and imaginary (out-of-phase or quadrature) components of the complex conductivity σ^*, respectively, and are given by

$$\sigma^* = \sigma' + i\sigma'' = |\sigma|\exp(i\varphi), \tag{4}$$

with the magnitude of the conductivity written as $|\sigma^*| = (\sigma'^2 + \sigma''^2)^{1/2}$ and the phase lag, φ, given by $\tan\varphi = \sigma''/\sigma'$. In the frequency range 0.1 - 1000 Hz, in-phase and quadrature conductivities are only slightly frequency dependent because grain polarization occurs over a broad range of scales (Vinegar and Waxman, 1984; Revil, 2012, 2013). Complex conductivity is written as $\varepsilon^* = \varepsilon' + i\varepsilon''$. By neglecting the polarization of water molecules (above 1 GHz) and Maxwell Wagner polarization, one can safely neglect the imaginary component of the dielectric constant, whereby $\varepsilon^* \approx \varepsilon'$, thus giving rise to the approximation $\sigma_{eff} \approx \sigma'(\omega)$.

In-phase conductivity

Revil (2013) developed a new model to describe the complex conductivity of clayey materials using a volume-average approach. According to Revil (2013) and assuming volumetric averaging to describe effective conductivity, the in-phase conductivity σ' (in S m^{-1}) of porous materials is given as a function of pore water conductivity σ_w (in S m^{-1}) by the expression

$$\sigma' = \frac{1}{F}\left\{ S_w^{\,n}\sigma_w + S_w^{\,p}\left(\frac{F-1}{F\phi}\right)\rho_S\left[\beta_{(+)}(1-f) + \beta_{(+)}^{S} f\right]\mathrm{CEC}\right\}, \quad (5)$$

where F (dimensionless) denotes the (intrinsic) formation factor for resistivity. It is related to connected porosity ϕ by Archie's equation $F = \phi^{-m}$ where m (dimensionless) denotes the porosity exponent. The total connected porosity entering Archie's law does not distinguish between kerogen and matrix porosities. The parameters n and p (both dimensionless) denote the second Archie exponent (saturation exponent) and the saturation exponent for surface conductivity, respectively (with p=n-1 as introduced by Vinegar and Waxman, 1984 and demonstrated by Revil, 2013, using a volume-averaging approach), f denotes the fraction of counterions in the Stern layer (see Leroy et al., 2008 and Revil, 2012, for discussion for sand

and clayey materials), ρ_S denotes mass density of the solid phase (typically 2650±50 kg m^{-3} for the crystalline framework of clay minerals), $\beta_{(+)}$ is the mobility of counterions in the diffuse layer, and $\beta^S_{(+)}$ is the mobility of counterions in the Stern layer (both in $m^2s^{-1}V^{-1}$). For clay minerals, the mobility of counterions in the diffuse layer is equal to the mobility of the same counterions in bulk pore water (e.g., $\beta_{(+)}(Na^+, 25°C) = 5.2\times10^{-8}$ $m^2s^{-1}V^{-1}$, see Revil, 2012). Mobility of counterions in the Stern layer is substantially smaller and equal to $\beta^S_{(+)}(25°C, Na^+) = 1.5 \times 10^{-10}$ $m^2s^{-1}V^{-1}$ for clay minerals (Revil, 2012, 2013). The acronym CEC (expressed in C kg^{-1}) denotes cation exchange capacity of the material. In equation 5, S_w denotes saturation of the water phase (S_w =1 for a water-saturated material).

Because the formation factor is generally much higher than unity for tight formations (F>>1), equation 5 can be written as

$$\sigma' \approx \frac{1}{F} {S_w}^n \sigma_w + {S_w}^p \left(\frac{1}{F\phi}\right) \rho_S \left[\beta_{(+)}(1-f) + \beta^S_{(+)} f\right] \mathrm{CEC}. \quad (6)$$

The second additive term in this last equation corresponds to the surface conductivity σ_S. Equation 6 is also very close to the equation proposed by Revil et al. (1996) (their equation 15) for water-saturated doleritic core samples from the oceanic crust. A simple generalization of the above expression to anisotropic media yields the following expression for the in-phase conductivity tensor:

$$\boldsymbol{\sigma}' = \sigma_{ij}' \mathbf{x}_i \otimes \mathbf{x}_j, \quad (7)$$

$$\mathbf{F} = F_{ij} \mathbf{x}_i \otimes \mathbf{x}_j, \quad (8)$$

$$\mathbf{T} = T_{ij} \mathbf{x}_i \otimes \mathbf{x}_j, \quad (9)$$

and

$$\sigma_{ij}' \approx F_{ij} \left({S_w}^n \sigma_w\right) + T_{ij} {S_w}^p \rho_S \left[\beta_{(+)}(1-f) + \beta^S_{(+)} f\right] \mathrm{CEC}, \quad (10)$$

where $\mathbf{x}_i$ (i =1, 2, 3) denote the basis vectors of the Cartesian frame of reference ($\mathbf{x}_i \cdot \mathbf{x}_j = \delta_{ij}$ where δ_{ij} denotes the Kronecker delta), $\mathbf{a} \otimes \mathbf{b}$ represents the tensorial product between vectors **a** and **b**, F_{ij} denotes the components of the (symmetric second-rank) formation factor tensor for the conductivity **F**, and T_{ij} denotes the components of the (symmetric second-rank) tortuosity tensor of the pore space **T**. We designate **T** as a connectivity tensor, as its entries vary between 0 and 1 and represent the inverse of the tortuosity defined in the isotropic case (see Bear, 1988; Bear and Bachmat, 1991; Bear and Cheng, 2010). Usually, in clayey materials, one has $\beta_{(+)}(1-f) >> \beta_{(+)}^{S} f$ (Revil, 2012, 2013) whereby the last term of equation 10 can be further simplified to $T_{ij} S_w^{\,p} \rho_S \beta_{(+)} (1-f)\mathrm{CEC}$. Our model also assumes that the saturation exponent remains more or less the same in different directions. We will see later that this assumption agrees well with the experimental data.

The components of the conductivity formation tensor and connectivity tensor are related to each other by

$$F_{ij} = T_{ij} \phi . \tag{11}$$

Therefore, both conductivity formation factor and connectivity tensors share the same eigenvectors and, for the case of TI materials, the anisotropy ratio should be the same for bulk and surface conductivities. This important technical point will be experimentally verified in the last section of the present paper. In the isotropic case, one has

$$F_{ij} = (1/F)\delta_{ij} , \tag{12}$$

whereby

$$T_{ij} = (1/F\phi)\delta_{ij} . \tag{13}$$

Note that the tortuosity, τ, of the pore space in the isotropic case ($\tau \geq 1$) is defined as (e.g., Pride, 1994; Zhang and Knackstedt, 1995; Clennell, 1997; Sevostianova et al., 2010; Zhang and Sherer, 2012)

$$F = \frac{\tau}{\phi} , \tag{14}$$

$$\tau = F\phi = \phi^{1-m}, \quad (15)$$

where we have used Archie's equation ($F = \phi^{-m}$ with m designating the porosity exponent, Archie, 1942). The iso-conductivity point designates the point characterized by a macroscopic conductivity equal to the pore water conductivity (e.g., Revil et al., 1998). Above the iso-conductivity point, surface and quadrature conductivity share the same bulk tortuosity, as discussed, for instance, by Revil and Glover (1997); the reason is the following: above the iso-conductivity point, surface conductivity is only a perturbation to the pore water conductivity and the electrical field is controlled by the conductivity of the pore space (see discussion in Bernabé and Revil, 1995, and Revil and Glover, 1997). Such a behavior explains why the same tortuosity is applied to the bulk and surface conductivities in the "high-salinity" regime. When surface conductivity dominates, conductivity is controlled by the distribution of surface conductance, and the tortuosity of electrical current along the surface of the minerals is different (usually higher) from that in pore water (see Bernabé and Revil, 1995, for a pore network modeling of this effect).

Quadrature conductivity

The expression for quadrature conductivity obtained by Revil (2013) is

$$\sigma'' \approx S_w^{\,p}\left(\frac{1}{F\phi}\right)\rho_S \beta_{(+)}^{S} f\,\mathrm{CEC}. \quad (16)$$

We emphasize that the explicit dependence of quadrature conductivity on the inverse of the product $(F\phi)$ and on water saturation raised to the power $p = n$ -1 are consistent with findings by Vinegar and Waxman (1984) and Revil (2013). However equation 16 is based on a volume averaging procedure while Vinegar and Waxman's (1984) model is predominantly based on empirical considerations. Equation 16 agrees with Vinegar and Waxman's (1984) observations in the laboratory (see also Revil, 2012 and 2013 for some tests using additional

data sets). Field observations also confirm an effect of oil saturation upon quadrature conductivity (e.g., Olhoeft, 1986; Deceuster and Kaufmann, 2012).

The generalization of equation 16 to anisotropic media is straightforward, namely,

$$\boldsymbol{\sigma}'' = \sigma_{ij}'' \mathbf{x}_i \otimes \mathbf{x}_j , \tag{17}$$

and

$$\sigma_{ij}'' = T_{ij} S_w^{\,p} \rho_S \beta_{(+)}^S f_M \,\mathrm{CEC} . \tag{18}$$

where $\boldsymbol{\sigma}''$ denotes the complex conductivity tensor and σ_{ij}'' identifies the entries of this tensor. Our model also assumes that the *p*-exponent remains more or less the same in different directions ike for the saturation exponent. We will see later that this assumption agrees well with the experimental data.

The complex conductivity tensor is defined as,

$$\boldsymbol{\sigma}^* = \sigma_{ij}^* \mathbf{x}_i \otimes \mathbf{x}_j , \tag{19}$$

and

$$\sigma_{ij}^* = \sigma_{ij}' + i\sigma_{ij}'' , \tag{20}$$

where σ_{ij}' and σ_{ij}'' are given by equations 10 and 18, respectively.

Dielectric constant

The remaining component of the generalized model is the (true or high-frequency) dielectric constant of porous material. In what follows, the notation ε_w and ε_o designates the dielectric constant of the water and oil phases, respectively, while ε_S designates the dielectric constant of the solid phase. By invoking volume averaging, Revil (2013) obtained

$$\varepsilon' = \frac{1}{F}\left[S_w^{\,n} \varepsilon_w + (1 - S_w^{\,n})\varepsilon_o + (F-1)\varepsilon_S \right], \tag{21}$$

which can be simplified as

$$\varepsilon' = \frac{1}{F}\left[S_w{}^n \varepsilon_w + (1 - S_w{}^n)\varepsilon_o \right] + \varepsilon_S \tag{22}$$

for tight formations (recalling that F>>1). For anisotropic formations, equation 22 can be generalized as

$$\boldsymbol{\varepsilon} = \varepsilon_{ij} \mathbf{x}_i \otimes \mathbf{x}_j , \tag{23}$$

and

$$\varepsilon_{ij} = F_{ij}\left[S_w{}^n \varepsilon_w + (1 - S_w{}^n)\varepsilon_a \right] + \varepsilon_{ij}^S , \tag{24}$$

where ε_{ij}^S designates the components of the dielectric tensor of the solid phase $\boldsymbol{\varepsilon}_S = \varepsilon_{ij}^S{}'' \mathbf{e}_i \otimes \mathbf{e}_j$. Note that the eigenvectors of this tensor correspond to the anisotropy of the solid matrix, and may be different from the eigenvectors associated with the tortuosity tensor of the pore space. In tight formations, the entries of $\boldsymbol{\varepsilon}_S$ can be obtained by taking the core sample *in vacuo,* and measuring the components of the dielectric tensor in different directions. That said, we expect that in most conditions the eigenvectors of the dielectric constant to be aligned with the eigenvectors of the complex conductivity tensor. Josh et al. (2012) observed that the anisotropy ratio can reach a factor 5 for the high frequency dielectric constant (>0.1 GHz).

Ampère's law in anisotropic media

The general form of Ampère's law in tight formations is, therefore, given by

$$\nabla \times \mathbf{H} = \left[\boldsymbol{\sigma}_{eff} - i\omega \boldsymbol{\varepsilon}_{eff} \right] \cdot \mathbf{E} , \tag{25}$$

$$\boldsymbol{\varepsilon}_{eff} = \varepsilon_{ij}^{eff} \mathbf{x}_i \otimes \mathbf{x}_j , \tag{26}$$

$$\boldsymbol{\sigma}_{eff} = \sigma_{ij}^{eff} \mathbf{x}_i \otimes \mathbf{x}_j , \tag{27}$$

$$\sigma_{ij}^{eff} \approx \sigma_{ij}' \approx F_{ij}\left(S_w{}^n \sigma_w \right) + T_{ij} s_w{}^p \rho_S \beta_{(+)} (1 - f)\mathrm{CEC} . \tag{28}$$

and

$$\varepsilon_{ij}^{eff} = F_{ij}\left[S_w{}^n\varepsilon_w + (1-S_w{}^n)\varepsilon_a\right] + \varepsilon_{ij}^S - \frac{1}{\omega}T_{ij}S_w{}^p\rho_S\beta_{(+)}^S f_M \,\mathrm{CEC}\,. \tag{29}$$

The above equations neglect an important polarization mechanism in the intermediate frequency range (0.1 MHz-100 MHz), often referred to as Maxwell-Wagner polarization. This polarization mechanism is related to the discontinuity of displacement currents at interfaces of porous composites. According to Revil (2013), Maxwell-Wagner polarization is not negligible but not as important as often emphasized in the technical literature. We acknowledge that this mechanism should be included in future studies.

In the next section, we discuss the properties of the tortuosity and formation factor tensors and describe their definition for anisotropic porous material.

FORMATION FACTOR AND TORTUOSITY TENSORS

We first invoke the definition of two textural parameters, F and Λ, defined in a number of previous studies (e.g., Johnson et al., 1986; Avellaneda and Torquato 1991; Pride, 1994). The canonical boundary value problem for the normalized potential Γ of a cylindrical representative elementary volume of porous material of length L can be written as

$$\nabla^2\Gamma = 0 \text{ in } V_p, \tag{30}$$

$$\hat{\mathbf{n}}_s \cdot \nabla\Gamma = 0 \text{ on } S, \tag{31}$$

and

$$\Gamma = \begin{cases} L \text{ at } z = L \\ 0 \text{ at } z = 0 \end{cases} \text{ on } S, \tag{32}$$

where z denotes the distance along the axis of the cylindrical core. In the above equations, $\hat{\mathbf{n}}_s$ denotes the unit vector normal to the pore water/mineral interface, S (directed from the pore to the solid phase, Figure 1), and V_p designates pore volume. Boundary conditions defining the normalized potential Γ are representative for the injection of an electrical current into a rock

sample in the absence of surface conduction along the pore/water interface (see Johnson et al., 1986, Avellaneda and Torquato, 1991). The formation factor F is defined as (Johnson et al., 1986)

$$\frac{1}{F} = \frac{1}{V}\int_{V_p} |\nabla\Gamma|^2 \, dV_p \,, \tag{33}$$

where V is the total volume of the considered representative elementary volume. Similarly, the tortuosity of the pore space is defined by Pride (1994) as

$$\frac{1}{\tau} = 1 + \frac{\hat{\mathbf{z}}}{V_p} \cdot \int_S \hat{\mathbf{n}}_s \Gamma dS \,, \tag{34}$$

where the integration is performed over the surface of the grain/pore water interface, S. Similarly, surface tortuosity could be defined from the surface formation factor introduced by Revil and Glover (1997). However, such surface tortuosity is required in our model for the reasons explained above.

In what follows, we designate $\mathbf{e} = -\nabla\Gamma$ the normalized electrical field (local electrical field divided by the norm of the macroscopic imposed field). The previous set of definitions can be readily generalized to the anisotropic case in the following manner:

$$\mathbf{F} = \frac{1}{V}\int_{V_p} \mathbf{e} \otimes \mathbf{e} \, dV_p \,, \tag{35}$$

and

$$\mathbf{T} = \frac{1}{V_p}\int_{V_p} \mathbf{e} \otimes \mathbf{e} \, dV_p \,, \tag{36}$$

Equations 35 and 36 show that **F** and **T** are symmetric.

Tortuosity and formation factor tensors can also be written in terms of three eigenvalues T^i (positive and less than one) for **T** and $(1/F^i)$ (F_i positive and greater than one) for **F** and the eigenvectors $\mathbf{t}^i$ as

$$\mathbf{T} = \sum_{i=1}^{3} T^i \mathbf{t}^i \otimes \mathbf{t}^i \,, \tag{37}$$

and

$$\mathbf{F} = \sum_{i=1}^{3} \left(\frac{1}{F^i} \right) \mathbf{t}^i \otimes \mathbf{t}^i \,. \tag{38}$$

For isotropic media, the above formulations simplify to the classical tortuosity and formation factor (see Bear, 1988 for a description of the connectivity tensor),

$$T^1 = T^2 = T^3 = \frac{1}{\tau}, \tag{39}$$

and

$$F^1 = F^2 = F^3 = \frac{\tau}{\phi}. \tag{40}$$

The inverses of connectivity and conductivity formation factor tensors are obtained through the expressions

$$\mathbf{T}^{-1} = T_{ij}^{-1} \mathbf{e}_i \otimes \mathbf{e}_j = \sum_{i=1}^{3} \frac{1}{T^i} \mathbf{t}^i \otimes \mathbf{t}^i \,, \tag{41}$$

and

$$\mathbf{F}^{-1} = F_{ij}^{-1} \mathbf{e}_i \otimes \mathbf{e}_j = \sum_{i=1}^{3} F^i \mathbf{t}^i \otimes \mathbf{t}^i \,, \tag{42}$$

respectively. Note that for TI media, with (1,2) being the symmetry plane, one has $F^1 = F^2 \neq F^3$ and $T^1 = T^2 \neq T^3$. The anisotropy ratio is defined as $\lambda = F^3 / F^1 = T^3 / T^1$. Mudrock formations are expected to have a petrofabric obeying this type of symmetry. In such a case, our model predicts that the anisotropy ratio for in-phase conductivity should be the same as that of quadrature conductivity. In addition, the anisotropy ratio for formation factor should be the same for both surface and quadrature conductivites. We verify this prediction in the last section of the paper.

INFLUENCE OF ORGANIC MATTER AND KEROGEN CONTENT ON COMPLEX CONDUCTIVITY

As emphasized above, CEC plays a critical role in controlling not only the surface conductivity of clayey materials (Waxman and Smits, 1968), but also their quadrature conductivity (Vinegar and Waxman, 1984; Revil, 2012), or equivalently the low-frequency dielectric constant (Josh et al., 2012; Revil, 2013). This behavior is illustrated in Figure 2 for the quadrature conductivity of porous siliciclastic materials.

In our model, quadrature conductivity can be expressed as a function of CEC as

$$\boldsymbol{\sigma}'' = -\mathbf{b}\,\mathrm{CEC}_M\,, \tag{43}$$

and

$$\mathbf{b} = \beta_{(+)}^{S} f \rho_S \mathbf{T}\,. \tag{44}$$

For isotropic and kerogen-free materials, Figure 2 plots equation 43 with $\mathbf{b} = b\mathbf{I}$ ($\mathbf{I}$ denotes the identity 3×3 matrix) and $b = 2.38\times10^{-7}$ S kg C^{-1} m^{-1} ($F\phi$ has been replaced by a tortuosity of 3/2, roughly the tortuosity of a path around spherical grains) against measurements. For fine-grained shales, tortuosity is expected to be much higher than 1.5. The last section of this paper shows that the tortuosity of bulk pore space of a mudrock can exceed 100. In turn, this behavior implies that for the same CEC, the quadrature conductivity of a mudrock is much smaller than for the case of a porous shaly sand (typically 1.5 to 3, see Vinegar and Waxman, 1984). Such an observation will also be discussed in the last section of the paper.

In Figure 3, we also test the fact that, according to our model, the salinity dependence of quadrature conductivity is governed by the salinity dependence of the partition coefficient, *f*. This salinity dependence is discussed in Appendix A. As *f* increases with salinity, we expect the magnitude of the quadrature conductivity to increase with salinity in agreement

347 with what is shown in Figure 3 (see also Weller et al., 2011; Revil and Skold, 2012; Weller
348 and Slater, 2012; and Revil et al., 2013).

349 In mudrocks (or in soils rich in organic matter), one may wonder about the role of
350 kerogen or humic substances on complex conductivity. Kerogens are commonly present in
351 high concentration in mudrocks, which clearly indicates they are potential source rocks for
352 hydrocarbon deposits. However, this also indicates the solid phase comprises an additional
353 component, which is characteristically distinct from the mineral rock matrix and should be
354 accounted for in the analysis of complex conductivity.

355 To understand the CEC or specific surface area (SSA or S_{Sp}) of kerogen-rich rocks, it
356 is important to emphasize the CEC or specific surface area of the kerogen itself. Few
357 published works have considered the CEC / specific surface area measurements in oil or gas
358 mudrocks. In that context, Derkowski and Bristow (2012) addressed the important question
359 of whether sedimentary organic matter (mostly kerogen) in oil and gas mudrocks exhibits
360 similar properties to those of organic matter found in soils. Indeed, during burial, organic
361 matter has been subjected to pressure and temperature changes and these changes can alter the
362 original properties.

363 Helling et al. (1964) reported a CEC for organic matter in soils, for pH between 6 to 8,
364 in the range 1.6 to 2.1 meq g^{-1} [1meq g^{-1} = 96,320 C kg^{-1}, equating to $(1.5\text{-}2.0)\times10^5$ C kg^{-1} in
365 SI units]. Kaiser et al. (2007) reported CEC values for organic matter of soils in the order of
366 $(0.3\text{-}3.5)\times10^5$ C kg^{-3} at pH 7. These values are extremely high and similar to the cation
367 exchange capacity of smectite (about 1 meq g^{-1}, 10^5 C kg^{-3}, e.g., Revil, 2012), the clay
368 mineral with the highest cation exchange capacity. Humus is known to have a CEC greater
369 than smectite. This cation exchange capacity is explained by the high reactivity of the surface
370 of organic matter as well as by the existence of isomorphic substitution in the organic
371 macromolecules themselves (such as with smectite). Figure 4 shows different reactive sites

372 on the surface of organic matter that are responsible for their high CEC. At near neutral pH
373 values, the number of electrical charges per unit surface area can be determined as the ratio of
374 total charge per unit mass CEC to total surface area per unit mass SSA; for humus: 559 cMol
375 kg^{-1} (5.6×10^5 C kg^{-3}) by 7.2 x 10^5 m^2 kg^{-1}; this yields a surface charge of 0.78 C m^{-2} (about 5
376 elementary charge per nm^2), a value that is approximately twice that of clays (e.g., Woodruff
377 and Revil, 2011).

378 The CEC and specific surface area of soil or oil mudrocks can therefore be written as

379 $$\mathrm{CEC} = \sum_{i=1}^{N} \chi_i \mathrm{CEC}_i \,, \tag{46}$$

380 and

381 $$\mathrm{S}_{sp} = \sum_{i=1}^{N} \chi_i \mathrm{S}_{sp,i} \,, \tag{47}$$

382 where N is the number of the mineral phases (including kerogen in oil mudrocks or organic
383 matter in soils) and χ_i denotes the mass fraction of the i –th mineral with respect to the total
384 mass of dry solid. In oil mudrocks, CEC can be expected to be dominated by clay minerals
385 and kerogen, whereby

386 $$\mathrm{CEC} = \chi_\mathrm{K}\mathrm{CEC}_\mathrm{K} + \chi_\mathrm{I}\mathrm{CEC}_\mathrm{I} + \chi_\mathrm{S}\mathrm{CEC}_\mathrm{S} + \chi_\mathrm{Ke}\mathrm{CEC}_\mathrm{Ke} \,, \tag{48}$$

387 and

388 $$\mathrm{S}_{sp} = \chi_\mathrm{K}\mathrm{S}_{sp,\mathrm{K}} + \chi_\mathrm{I}\mathrm{S}_{sp,\mathrm{I}} + \chi_\mathrm{S}\mathrm{S}_{sp,\mathrm{S}} + \chi_\mathrm{Ke}\mathrm{S}_{sp,\mathrm{Ke}} \,, \tag{49}$$

389 where the subscripts K, I, and S refer to kaolinite, illite, and smectite, respectively, while Ke
390 refers to kerogen. There are five types of kerogen defined in the literature: Type I (sapropelic,
391 formed from protein and lipids of mostly algae), Type II (Planktonic, formed from lipids of
392 plankton deposited under reducing conditions), Type II-S (similar to type II with a high sulfur
393 content), Type III (humic, from terrestrial plants), and Type IV (contains mostly decomposed

394 organic matter). It is possible that the CEC and SSA of kerogen may depend on the type and
395 maturity of kerogen as well.

396 The CEC of humic matter and kerogen can be related to the quantity of carbon in oil
397 mudrocks. For soils that are rich in organic matter, it is known that cation exchange capacity
398 is highly correlated with carbon content (Figure 5). Therefore, one could expect a correlation
399 between TOC (total amount of organic carbon content in weight %) of kerogen and cation
400 exchange capacity of the material. That said, experimental results available in the literature
401 are conflicting (see the discussion in Derkowski and Bristow, 2012). The CEC of kerogen is
402 believed to be very small compared to the CEC of organic matter in soils because all the
403 available exchangeable sites in functional groups shown in Figure 4 may have been
404 polymerized during burial (see Vandenbroucke and Largeau, 2007). Derkowski and Bristow
405 (2012) indicate that the thermal treatment used prior to CEC measurements can reactivate
406 some of these functional sites (possibly through the deprotonation of carboxylic acids) and
407 lead to a CEC associated with kerogen which may explain conflicting results found in the
408 literature. Derkowski and Bristow (2012) observed an inverse relationship between kerogen
409 maturity and the amount of carboxylic groups. It then follows that immature kerogen has
410 greater susceptibility to thermal activation. Therefore, the thermal treatment applied to less
411 mature kerogen may substantially increase the CEC of the material, as well as surface
412 conduction and quadrature conductivity (polarization).

413 In summary, we believe that the CEC of kerogen can be neglected in the evaluation of
414 the quadrature conductivity of hydrocarbon-bearing tight mudrocks (Derkowski and Bristow,
415 2012) but not the specific surface area, which can be very high. Derkowski and Bristow
416 (2012) reported a specific surface area in the range from 700 to 920 m^2 g^{-1} for kerogen
417 extracted from the mature Red Bird and Monterey formations. This represents a range of
418 values very similar to that measured for smectite (e.g., Woodruff and Revil, 2011). For the

419 Woodford formation, Derkowski and Bristow (2012) measured the excess specific surface
420 area not accounted for by clay minerals. As shown in Figure 6, such an excess surface area is
421 correlated with total amount of organic carbon content (in weight %). The relationship can be
422 written as

423 $$S_{sp}(\text{Kerogen}) = a\,\text{TOC}(\%)\,, \tag{50}$$

424 where $a \approx 10$. For pure kerogen, the above expression yields [TOC(%) =100] a specific
425 surface area of 1000 $m^2\ g^{-1}$, which is only slightly higher than values given above. Therefore,
426 specific surface area is given by

427 $$S_{sp} = \chi_{Clay} S_{sp,\text{clay}} + S_{sp,\text{Ke}}\,\text{TOC}\,, \tag{51}$$

428 where TOC is expressed in mass fraction (in %). However, it is unclear at this point whether
429 kerogen would impact the quadrature conductivity through its surface area. In principle, if
430 there is no Stern layer associated with kerogen (no reactive sites), presence of kerogen in oil
431 and gas mudrocks should have no impact on quadrature conductivity. Therefore if the
432 specific surface area is used to assess the quadrature conductivity, the former should be
433 corrected for the contribution of kerogen. The TOC content might also change the tortuosity
434 of the porous body and indirectly affect the bulk conductivity. Furthermore, if bitumen is
435 present, the polar components might contribute to the surface conductivity. However, these
436 effects need to be verified by experimental evidence.
437

438 ## COMPARISON TO EXPERIMENTAL DATA

439

440 **Material and methods**

441 This section analyzes the complex conductivity of two Bakken core samples. The
442 Bakken formation is a Late Devonian Early Mississippian shale (deposited approximately 360
443 millions of years ago) located in the Williston Basin, underlying parts of Montana, North

444 Dakota, and Saskatchewan. Sample A was acquired at a depth of 2630 m while Sample B was
445 acquired at 3098 m. The deeper sample, Sample B, is from the higher-temperature, central
446 portion of the Williston Basin, whereas the second core sample is from the basin's margin.
447 Table 1 summarizes the properties of the two core samples. Porosity was measured by
448 hydrogen adsorption, which does not account for the percentage weight (wt%) of kerogen;
449 20wt% kerogen results in 40-70 vol% kerogen, depending on the density of kerogen (Prasad
450 et al., 2011). Average non-kerogen porosity in Bakken shale samples is approximately 3%.
451 Spectral induced polarization measurements were performed using an apparatus
452 developed at the Central Laboratory for Electronics, ZEL, at the Forschungszentrum Jülich, in
453 Germany by Zimmermann et al. (2008). Various tests of this impedance meter have been
454 documented by Revil and Skold (2011) and will not be repeated here. Electrodes used were
455 sintered $Ag/AgCl_2$ 2 mm pellet electrodes for voltage measurements (http://www.science-
456 products.com/Products/CatalogG/IVM-$AgAgCl_2$-Pellets/ivm.html), and transcutaneous
457 electrical nerve stimulation (TENS) adhesive electrodes
458 (https://www.djoglobal.com/products/chattanooga/dura-stick-ii-self-adhesive-electrodes) for
459 current injection (see Figure 7 for a description of the position of the electrodes).
460 The Bakken samples were saturated with three pore-water solutions of varied salinity
461 derived from an equilibrium solution obtained by saturating (distilled) DI water with a soluble
462 mineral fraction of pulverized core fragments. A low-salinity limit of 0.5 mM was estimated
463 as the equilibrium concentration of NaCl. Solutions were also prepared for 0.05 M and 0.5 M.
464 The samples were initially saturated with equilibrium water under sequential pressurizations
465 up to 10.3 MPa (1500 psi), and re-saturated with the remaining solutions in two stages.
466 Spectral induced polarization acquisitions were made at each of the three stages. Due to the
467 low diffusion coefficient for the NaCl solution in the samples, approximately 10^{-11} m^2s^{-1}
468 (Revil et al., 2005), the equilibration time at each stage is in the order of several weeks (the

469 average radius of the cylindrical samples is 0.010 m, yielding 1×10^{-4} / 2.5×10^{-11} = 4×10^{6} s ≈
470 46 days). The brine is degassed prior to the saturation. The saturated samples are immersed
471 in the respective equilibrium solution and stored at low pressure close to vacuum conditions.
472 Complex spectra of the eigenvalues of the electrical impedance tensor were obtained
473 directly by following the single-component polarization protocol with the 4 electrode
474 impedance spectroscopy method developed by Zimmermann et al. (2008). The Bakken B
475 specimens are cylindrical cores with a radius of 12.6 mm and heights 38.3 mm and 30.8 mm
476 for the in-plane and transverse directions, respectively; geometric factors were obtained
477 numerically using a Comsol Multiphysics simulator. We perform the measurements at
478 laboratory temperature and pressure; we coated the samples in quick dry nail polish to prevent
479 both evaporation at the core surface, as well as impose an insulating boundary, constituting a
480 closed electrical system for the measurements. With this approach, no sample holder is
481 required. The coating is easily removed with acetone to maximize surface exposure for
482 subsequent pressurizations. Spectral complex conductivity tensors were determined from the
483 measured directional impedances of the samples. Table 2 summarizes the in-phase and
484 quadrature conductivity of the two core samples at 1 Hz.
485 We also performed spectral induced polarization at five different stages, referred to
486 below as stages I through V, during the pressurized saturation sequence, capturing unsaturated
487 measurements at different water contents for Sample B. The samples were pressurized at
488 increasing sequential maximum confining (hydrostatic) pressures of 0.69 MPa, 3.45 MPa,
489 6.89 MPa, and 10.34 MPa. Stages I and II were completed in two successive 24 hour periods,
490 and stages III and IV in successive 48 hour periods. An additional measurement was made
491 after 30 days to represent the final saturation state, stage V (the datasets of stages IV and V
492 are equivalent, evidencing full saturation of the sample; the stage V measurements are used in

493 our analysis). The water content is determined through gravimetric monitoring at each
494 saturation stage.
495
496 **Results under saturated conditions**

497 Figure 8 shows the raw data for the phase. The tangent of the phase angle is defined
498 as the ratio of quadrature conductivity to in-phase conductivity. Figure 8 reveals only a fair
499 agreement between the phases measured in the in-plane and trasnverse directions of the core
500 samples at low frequencies. The magnitude of the phase increases slightly with frequency
501 below 100 Hz and faster above 100 Hz. The polarization of the electrical double layer is
502 expected to dominate the response of the quadrature conductivity below 100 Hz, while above
503 100 Hz, the response is partly controlled by the true dielectric polarization of the material
504 with some influence from the Maxwell-Wagner polarization (see Revil, 2013) and possibly
505 some electromagnetic coupling effects.

506 The complex conductivity spectra are plotted as a function of frequency for the three
507 salinities in Figure 9 for Sample A, and in Figure 10 for Sample B. In-phase conductivity
508 data display only weak dependence with respect to frequency as already observed for other
509 clay-rich materials (see Vinegar and Waxman, 1984; Slater and Lesmes, 2002; Revil, 2012).
510 Quadrature conductivity spectra exhibit a plateau at low frequencies and an increase in
511 magnitude at high frequencies due to Maxwell-Wagner polarization and true dielectric
512 polarization (Revil, 2013).

513 We first test our prediction regarding anisotropy ratio for in-phase and quadrature
514 conductivities (see Figure 11). The mean anisotropy ratio is 8.1±3.1 (N = 12, N: number of
515 measurements) for in-phase and quadrature conductivity data acquired together for the two
516 core samples (7.6±2.3, N = 6, for the in-phase conductivity and 8.5±3.8, N = 4, for the
517 quadrature conductivity). The anisotropy ratio is approximately the same for both in-phase
518 and quadrature conductivities. This behavior is consistent with the predictions of our model.

519 We now focus on the relationship between in-phase conductivity and pore water
520 conductivity of NaCl solutions. Electrical conductivity of water can be described using the
521 semi-empirical relation derived by Sen and Goode (1992), i.e.

522 $$\sigma_f(C_f;T) = (d_1 + d_2T + d_3T^2)C_f - \frac{d_4 + d_5T}{1 + d_6C_f}(C_f)^{3/2}, \quad (52)$$

523 where d_1 = 5.6, d_2 = 0.27, d_3 = -1.51x10^{-4}, d_4 = 2.36, d_5 = 0.099, d_6 = 0.214, σ_f is electrical
524 conductivity of water (in S m^{-1}), T is temperature (in °C) and C_f is salinity (in M, mol L^{-1}).
525 This relation yields pore water conductivities of 3.82 S m^{-1}, 0.49 S m^{-1}, and 0.0054 S m^{-1}.
526 Figure 11 shows the corresponding in-phase and quadrature conductivities as a function of
527 conductivity of pore water solution. The relationship between in-phase conductivity and pore
528 water conductivity is used to determine formation factor and surface conductivity in the in-
529 plane and transverse directions with respect to bedding plane. Table 3 reports the formation
530 factors and surface conductivities, together with the determination of Archie's porosity
531 exponent ($m = -\ln F / \ln\phi$ in the two directions) and tortuosity ($\tau = F\phi$). For Samples A and
532 B, the surface conductivity anisotropy ratios are 8.8±0.9 and 7.4±0.8, respectively. These
533 values are comparable to the anisotropy ratios for the quadrature conductivity, 6.3±0.7 and
534 6.8±0.8, respectively for Samples A and B.

535 The immature sample A may have higher clay content, which could explain the higher
536 surface conductivity than observed for sample B. Regarding quadrature conductivity, the in-
537 plane (I) and transverse (T) quadrature conductivities are given by

538 $$\sigma''(I) = -\frac{\beta^S_{(+)} f \rho_S}{\tau_I}\mathrm{CEC}_M, \quad (53)$$

539 and

540 $$\sigma''(T) = -\frac{\beta^S_{(+)} f \rho_S}{\tau_T}\mathrm{CEC}_M, \quad (54)$$

541 while surface conductivities in the in-plane and transverse directions are given by

$$\sigma_S(I) = \frac{\rho_S \beta_{(+)}(1-f)}{\tau_I} \mathrm{CEC}_M , \quad (55)$$

and

$$\sigma_S(T) = \frac{\rho_S \beta_{(+)}(1-f)}{\tau_T} \mathrm{CEC}_M , \quad (56)$$

respectively, where $\beta_{(+)}(\mathrm{Na}^+, 25°\mathrm{C}) = 5.2\times10^{-8}$ $\mathrm{m^2 s^{-1} V^{-1}}$) and $\beta^S_{(+)}(25°\mathrm{C}, \mathrm{Na}^+) = 1.5 \times 10^{-10}$ $\mathrm{m^2 s^{-1} V^{-1}}$ for clay minerals (Revil, 2012, 2013). We first determine the CEC using equations 53 and 54, and f close to 1. Very consistent values are obtained at high salinities with CEC = 2500 ± 300 C $\mathrm{kg^{-1}}$ for sample A and CEC = 1200 ± 300 C $\mathrm{kg^{-1}}$ for sample B. This behavior agrees with the known CEC of the Bakken shale, which is in the order of 10^{-2} to 10^{-1} meq $\mathrm{g^{-1}}$ (about 1000 to 10,000 C $\mathrm{kg^{-1}}$; data obtained from the North Dakota Industrial Commission, Department of Mineral Resources, Oil and Gas Division online subscription database, https://www.dmr.nd.gov/oilgas/subscriptionservice.asp). Using equations 55 and 56, we obtain f = 0.78±0.03 for Sample A and f = 0.99 for Sample B. The values of CEC and f obtained by our model are consistent with the expected their respective relationship to clay type, and may imply that sample A is richer in smectite and that Sample B is rich in kaolinite.

Figure 12 describes the impact of anisotropy and increase of tortuosity for the Bakken shale by comparison to shaly sands investigated by Vinegar and Waxman (1984) and the saprolites investigated by Revil et al. (2013). As predicted by our model, at given values of CEC and salinity, the magnitude of quadrature conductivity is expected to decrease with the increase of tortuosity and differ in the in-plane and transverse directions (respective to bedding. Tortuosity in the in-plane direction is also found to be much smaller than in the transverse direction. As shown in Figure 13a, differential compaction during burial is responsible for the formation of a bedding plane with the shale, thereby becoming a TI medium. In this case, we expect the tortuosity in the in-plane direction to be substantially

565 smaller than in the transverse direction (Figure 13b). Tortuosity in this case can also be
566 related to the aspect ratio of grains, as discussed in Mandelson and Cohen (1982). Other
567 published experimental works have reported very high tortuosities; for instance Revil et al.
568 (1996) reported tortuosities in the range of 2 to 46 for doleritic core samples. Zhang and
569 Scherer (2012, their Table 6) have reported electrical tortuosities in the range 2 to 118 for
570 tight shales. Values higher than 100 were obtained for very tight specimens with porosities
571 below 3%.
572
573 **Results Under Unsaturated Conditions**
574 Figure 14 shows the in-phase and quadrature conductivities of Sample B at different
575 saturations. It is clear from this figure that saturation does not change the anisotropy ratio of
576 the material. In-phase and quadrature conductivity data are plotted as a function of saturation
577 in Figure 15. Measurementsare fitted with a power-law relationship to determine the
578 saturation n-exponent and the p-exponent describing the saturation dependence of quadrature
579 conductivity. The first observation is that the n and p exponents do not exhibit significant
580 anisotropy (n = 2.7±0.4 in the in-plane direction and n = 2.4±0.3 in the transverse direction
581 and p = 1.8±0.1 in the in-plane direction and p = 1.4±0.2 in the transverse direction). Figure
582 16 reports the values of the two exponents together with the n and p exponents of isotropic
583 sedimentary materials (see Revil, 2013). All the data conform fairly well to the general trend
584 $p = n$-1.
585
586 ## CONCLUSIONS
587 We introduced a new petrophysical model to describe the complex electrical
588 conductivity tensor of oil mudrocks. The model accounts for anisotropy, saturation, porosity,
589 and cation exchange capacity/specific surface area of rocks. Verification experiments were

590 performed on two core samples from the Bakken formation. The following conclusions stem
591 from the work presented in this paper:

592 (1) In-phase electrical conductivity is controlled by a formation factor tensor while
593 quadrature conductivity is controlled by a tortuosity tensor of the bulk pore space. Both
594 tensors are interrelated through the connected porosity.

595 (2) The CEC of kerogen is believed to be very small in comparison to the CEC of
596 organic matter in soils. Indeed, because of diagenesis, all the exchangeable sites in the
597 functional groups of organic matter may have been polymerized; therefore, the surface of
598 kerogen may not impact both surface and quadrature conductivity of oil and gas mudrocks.

599 (3) Experimental data confirmed our model prediction that the anisotropy ratio is the
600 same for in-phase and quadrature conductivities. It was also confirmed that the anisotropy
601 ratio is the same for formation factor and surface conductivity. The anisotropy ratio for the
602 complex conductivity tensor is 8.1±3.1 for the two Bakken core samples. Our model predicts
603 an invariant phase angle for both in-plane (I) and transverse (T) measurements for all
604 frequencies. This behavior is only approximately shown by experimental data acquired at
605 low frequencies; additional data will be needed for verification.

606 (4) Measurements performed on two rock samples from the Bakken formation indicate
607 that our model provides a simple explanation for (a) the dependence of quadrature
608 conductivity on salinity and (b) the effect of increase of tortuosity on the decrease of the
609 magnitude of quadrature conductivity. The bulk tortuosity in the direction transverse to
610 bedding plane is found to be higher than 100. This very high value of tortuosity is likely
611 associated with the aspect ratio of grains.

612 (5) The decrease of saturation does not significantly change the degree of anisotropy
613 observed for the quadrature and in-phase conductivities under saturated conditions. It follows

614 that the *p*-exponent characterizing the saturation dependence of quadrature conductivity can
615 be related to the saturation exponent *n* by $p = n-1$.
616
617 **Acknowledgments.** This work was funded by The University of Texas at Austin's Research
618 Consortium on Formation Evaluation, jointly sponsored by Anadarko, Apache, Aramco,
619 Baker-Hughes, BG, BHP Billiton, BP, Chevron, China Oilfield Services, LTD.,
620 ConocoPhillips, ENI, ExxonMobil, Halliburton, Hess, Maersk, Marathon Oil Corporation,
621 Mexican Institute for Petroleum, Nexen, ONGC, Petrobras, Repsol, RWE, Schlumberger,
622 Shell, Statoil, Total, and Weatherford. We also than the Oclassh research project and its
623 sponsor (Chevron, Repsol, Whiting, Venoco, Shell, Aramco, Magrtek, and Hess). We thank
624 Egon Zimmermann for the construction of the impedance meter, Andreas Weller and an
625 anonymous referee for their constructive reviews of our manuscript, and the Associate Editor
626 for the speed of the review process.
627

REFERENCES

Archie, G.E., 1942, The electrical resistivity log as an aid in determining some reservoir characteristics: Transactions of the American Institute of Mining, Metallurgical, and Petroleum Engineers, **146**, 54–62.

Avellaneda, M., and S. Torquato, 1991, Rigorous link between fluid permeability, electrical conductivity, and relaxation times for transport in porous media: Physics of Fluids A, **3**, 2529–2540.

Bear J., 1988, Dynamics of Fluids in Porous Media, New York, Dover.

Bear J., and Y. Bachmat, 1991, Introduction to Modeling of Transport Phenomena in Porous Media, Dordrecht, Kluwer Academic Publishers.

Bear J., and Cheng A. H.-D., 2010, Modeling Groundwater Flow and Contaminant Transport. Theory and Applications of Transport in Porous Media, Dordrecht, Springer.

Bernabé, Y., and A. Revil, 1995, Pore-scale heterogeneity, energy dissipation and the transport properties of rocks: Geophysical Research Letters, **22**, no. 12, 1529-1552.

Bittar, M., J. Klein, R. Beste, G. Hu, M. Wu, J. Pitcher, C. Golla, G. Althoff, M. Sitka, V. Minosyan, and M. Paulk, 2009, A new azimuthal deep-reading resistivity tool for geosteering and advanced formation evaluation: SPE Reservoir Evaluation & Engineering, **12**, no. 2, 270-279

Clennell, B., 1997, Tortuosity: a guide through the maze: in Developments in Petrophysics, Geological Society Special Publication, **122**, published by The Geological Society, London, pp. 299-344.

Derkowski A. and T. Bristow, 2012, On the problems of total specific surface area and cation exchange capacity measurements in organic-rich sedimentary rocks: Clays and Clay Minerals, **60**, no. 4, 348–362.

652 Deceuster, J., and O. Kaufmann, 2012, Improving the delineation of hydrocarbon-impacted
653 soils and water through induced polarization (IP) tomographies: A field study at an
654 industrial waste land: Journal of Contaminant Hydrology, **136-137**, 25–42.
655 Flores Orozco, A., K. H. Williams, P. E. Long, S. S. Hubbard, and A. Kemna, 2011, Using
656 complex resistivity imaging to infer biogeochemical processes associated with
657 bioremediation of an uranium-contaminated aquifer: Journal of Geophysical Research,
658 **116**, G03001, doi:10.1029/2010JG001591.
659 Helling, C.S., G. Chesters, and R.B. Corey, 1964, Contribution of organic matter and clay to
660 soil cation exchange capacity as affected by the pH of the saturating solution: Soil Science
661 Society of America Journal, **28**, 517-520.
662 Johnson, D. L., T. J. Plona, and H. Kojima, 1986, Probing porous media with 1st sound, 2nd
663 sound, 4th sound and 3rd sound: in Physics and Chemistry of Porous Media, **II**, edited by
664 R. Jayanth, J. Banavar, and K. W. Winkler, 243–277, AIP, New York.
665 Josh, L. Esteban, C. Delle Piane, J. Sarout, D.N. Dewhurst, M.B. Clennell, 2012, Laboratory
666 characterization of shale properties: Journal of Petroleum Science and Engineering, **88–89**
667 107–124.
668 Kaiser, M., R.H. Ellerbrock, and H.H. Gerke, 2007, Cation exchange capacity and
669 composition of soluble soil organic matter fractions: Soil Science Society of America
670 Journal, **72**, 1278-1285, doi:10.2136/sssaj2007.0340.
671 Liang B., J. Lehmann, D. Solomon, J. Kinyangi, J. Grossman, B. O'Neill, J. O.
672 Skjemstad, J. Thies, F. J. Luizao, J. Petersen, and E. G. Neves, 2006, Black carbon
673 increases cation exchange capacity in soils: Soil Science Society of America Journal, **70**,
674 1719–1730.

675 Leroy, P., A. Revil, A. Kemna, P. Cosenza, and A. Ghorbani, 2008, Complex conductivity of
676 water-saturated packs of glass beads: Journal of Colloid and Interface Science, **321**, 103-
677 117.
678 Leroy P. and A. Revil, 2009, Spectral induced polarization of clays and clay-rocks: Journal of
679 Geophysical Research, **114**, B10202, doi:10.1029/2008JB006114.
680 Mandelson, K. S., and M. H. Cohen, 1982, The effect of grain anisotropy on the electrical
681 properties of sedimentary rocks: Geophysics, **47**, no. 2, 257-263.
682 Olhoeft, G.R., 1986, Direct detection of hydrocarbon and organic chemicals with ground
683 penetrating radar and complex resistivity: In Proc. National Water Wells Assoc. Conf. on
684 Hydrocarbons and organic chemicals in ground water: Prevention, detection and
685 restoration conference. Houston, Texas November 12-14, 284-305.
686 Prasad M., K.C. Mba, T.E. McEvoy, and M.L. Batzle, 2011, Maturity and impedance analysis
687 or organic-rich shales: Society of Petroleum Engineers Reservoir Evaluation Engineering,
688 **14**, no. 5, 533-543.
689 Pride, S. R., 1994, Governing equations for the coupled electromagnetics and acoustics of
690 porous media: Physical Review B, **50**, 15,678–15,696, doi:10.1103/PhysRevB.50.15678.
691 Revil, A., M. Darot, P.A. Pezard, and K. Becker, 1996, Electrical conduction in oceanic dikes,
692 Hole 504B, Ed. by Alt, J.C., Kinoshita, H., *et al*., Proc. ODP Sci. Res., 148: College
693 Station, TX (ODP), 297-305.
694 Revil, A., and P.W.J. Glover, 1997, Theory of ionic surface electrical conduction in porous
695 media, Physical Review B., **55**, no. 3, 1757-1773.
696 Revil, A., L.M. Cathles, S. Losh, J.A. Nunn, 1998, Electrical conductivity in shaly sands with
697 geophysical applications: Journal of Geophysical Research, **103**, no. B10, 23,925-23,936.

698 Revil, A., P. Leroy, and K. Titov, 2005, Characterization of transport properties of
699 argillaceous sediments. Application to the Callovo-Oxfordian Argillite: Journal of
700 Geophysical Research, **110**, B06202, doi: 10.1029/2004JB003442.
701 Revil, A., and N. Florsch, 2010, Determination of permeability from spectral induced
702 polarization in granular media: Geophysical Journal International, **181**, 1480-1498.
703 Revil A., and M. Skold, 2011, Salinity dependence of spectral induced polarization in sands
704 and sandstones, Geophysical Journal International: **187**, 813–824, doi: 10.1111/j.1365-
705 246X.2011.05181.x.
706 Revil, A., 2012, Spectral induced polarization of shaly sands: Influence of the electrical
707 double layer: Water Resources Research, **48**, W02517, doi:10.1029/2011WR011260.
708 Revil, A., K. Koch, and K. Holliger, 2012, Is it the grain size or the characteristic pore size
709 that controls the induced polarization relaxation time of clean sands and sandstones?
710 Water Resources Research: **48**, W05602, doi:10.1029/2011WR011561.
711 Revil A., and M. Skold, 2011, Salinity dependence of spectral induced polarization in sands
712 and sandstones: Geophysical Journal International: **187**, 813–824, doi: 10.1111/j.1365-
713 246X.2011.05181.x.
714 Revil, A., 2013, Effective conductivity and permittivity of unsaturated porous materials in the
715 frequency range 1 mHz - 1GHz: Water Resources Research, **49**,
716 doi:10.1029/2012WR012700.
717 Revil A., J.D. Eppehimer, M. Skold, M. Karaoulis, L. Godinez, and M. Prasad, 2013, Low-
718 frequency complex conductivity of sandy and clayey materials: in press in Journal of
719 Colloid and Interface Science.
720 Schwartz, N., and A. Furman, 2012, Spectral induced polarization signature of soil
721 contaminated by organic pollutant: experiment and modeling: Journal of Geophysical
722 Research, **117**, B10203, doi:10.1029/2012JB009543.

723 Sen, P.N., Goode, P.A., 1992. Influence of temperature on electrical conductivity of shaly
724 sands: Geophysics, **57**, 89–96.
725 Sevostianova E., B. Leinauer, I. Sevostianov, 2010, Quantitative characterization of the
726 microstructure of a porous material in the context of tortuosity: International Journal of
727 Engineering Science, **48**, 1693–1701.
728 Skold M., A. Revil, and P. Vaudelet, 2011, The pH dependence of spectral induced
729 polarization of silica sands: Experiment and modeling: Geophysical Research Letters, **38**,
730 L12304, doi:10.1029/2011GL047748.
731 Slater, L., and D. P. Lesmes, 2002, Electrical-hydraulic relationships observed for
732 unconsolidated sediments: Water Resources Research, **38**, no. 10, 1213,
733 doi:10.1029/2001WR001075.
734 Vandenbroucke, M. and C. Largeau, 2007, Kerogen origin, evolution and structure: Organic
735 Geochemistry, **38**, 719-833.
736 Vaudelet, P., A. Revil, M. Schmutz, M. Franceschi, and P. Begassat, 2011a, Changes in
737 induced polarization associated with the sorption of sodium, lead, and zinc on silica sands:
738 Journal of Colloid and Interface Science, **360**, 739-752.
739 Vaudelet, P., A. Revil, M. Schmutz, M. Franceschi, and P. Begassat, 2011b, Induced
740 polarization signatures of cations exhibiting differential sorption behaviors in saturated
741 sands: Water Resources Research, **47**, W02526, doi:10.1029/2010WR009310.
742 Veeken P. C. H., P. J. Legeydo, Y. A. Davidenko, E. O. Kudryavceva, S. A. Ivanov, and A.
743 Chuvaev, 2009, Benefits of the induced polarization geoelectric method to hydrocarbon
744 exploration, **74**, no. 2, B47–B59, 10.1190/1.3076607.
745 Vinegar, H. J., and M.H. Waxman, 1984, Induced polarization of shaly sands: Geophysics,
746 **49**, 1267-1287.

747 Waxman, M. H., and L. J. M. Smits, 1968, Electrical conductivities in oil bearing shaly sands:
748 Journal of the Society of Petroleum Engineers, **8**, 107–122.
749 Weller, A., K. Breede, L. Slater, and S. Nordsiek, 2011, Effect of changing water salinity on
750 complex conductivity spectra: Geophysics, **75**, no. 6, F315-F327.
751 Weller A. and L. Slater, 2012, Salinity dependence of complex conductivity of
752 unconsolidated and consolidated materials: Comparisons with electrical double layer
753 models: Geophysics, **77**, no. 5, D185–D198, doi: 10.1190/GEO2012-0030.1.
754 Weller, A., S. Nordsiek, and W. Debschütz, 2010, Estimating permeability of sandstone
755 samples by nuclear magnetic resonance and spectral-induced polarization: Geophysics,
756 75, no. 6, E215-E226.
757 Wilmanski, K., 2010, Tortuosity of porous media and its influence on properties of acoustic
758 waves (in Polish), IIIrd Conference: Mechanics of Inhomogeneous Media, Lagow
759 (Poland), 4-6 June 2010.
760 Woodruff, W. F., and A. Revil, 2011, CEC-normalized clay-water sorption isotherm: Water
761 Resources Research, **47**, W11502, doi:10.1029/2011WR010919.
762 Zargari, S., K Mba, E. Mattson, and M. Prasad, 2013, Organic maturity, elastic properties and
763 textural characteristics of self-resourcing reservoirs: in press in Geophysics.
764 Zhang J., and G. W. Scherer, 2012, Permeability of shale by the beam-bending method:
765 International Journal of Rock Mechanics & Mining Sciences, **53**, 179–191.
766 Zimmermann, E., A. Kemna, J. Berwix, W. Glaas, H.M Munch, and J.A. Huisman, 2008, A
767 high-accuracy impedance spectrometer for measuring sediments with low polarizability:
768 Meas. Sci. Technol., **19**, doi:10.1088/0957-0233/19/10/105603.
769 Zisser, N., and G. Nover, 2009, Anisotropy of permeability and complex resistivity of tight
770 sandstones subjected to hydrostatic pressure: Journal of Applied Geophysics, **68**, 356–
771 370.

772 Zisser, N., A. Kemna, and G. Nover, 2010a, Dependence of spectral induced polarization
773 response of sandstone on temperature and its relevance to permeability estimation: Journal
774 of Geophysical Research, **115**, B09214, doi:10.1029/2010JB007526.
775 Zisser N., A. Kemna A. and G. Nover, 2010b, Relationship between low-frequency electrical
776 properties and hydraulic permeability of low-permeability sandstones: Geophysics, **75**,
777 E131-E141, doi: 10.1190/1.3413260.
778 Zhang X., and M. A. Knackstedt, 1995, Direct simulation of electrical and hydraulic
779 tortuosity in porous solids: Geophysical Research Letters, **22**, no. 17, 2333–2336, Doi:
780 10.1029/95GL02230.
781 Zhang J. and G.W. Scherer, 2012, Permeability of shale by the beam-bending method:
782 International Journal of Rock Mechanics and Mining Sciences, **53**, 179–191.
783

Appendix A

We introduce a simple model to describe the dependence of salinity on the partition coefficient, *f*. Consider first the sorption of sodium in the Stern layer of clays and the dissociation of protons according to the following, simplified speciation model:

$$>SH^0 \Leftrightarrow >S^- + H^+, \tag{A1}$$

and

$$>S^- + Na^+ \Leftrightarrow >S^-Na^+, \tag{A2}$$

where >S designates the surface (amphoteric) sites attached to the crystalline framework, H^0 are protons (which are assumed to be immobile), while weakly sorbed Na^+ (which are known to keep their hydration layer) are assumed mobile in the Stern layer. Equilibrium constants for the reactions A1 and A2 are given by,

$$K_{Na} = \frac{\Gamma^0_{SNa}}{\Gamma^0_{S^-}\left[Na^+\right]^0}, \tag{A3}$$

and

$$K_H = \frac{\Gamma^0_{S^-}\left[H^+\right]^0}{\Gamma^0_{SH}}. \tag{A4}$$

The conservation equation for the surface species is given by,

$$\Gamma^0_S = \Gamma^0_{SNa} + \Gamma^0_{SH} + \Gamma^0_{S^-} + \Gamma^0_X, \tag{A5}$$

where Γ^0_S denotes the total surface site density (including charge associated with isomorphic substitutions in the crystalline framework), Γ^0_{SNa}, $\Gamma^0_{S^-}$, and Γ^0_{SH} designate the surface charge density of the sites $>S^-Na^+$, $>S^-$, and $>SH^0$, respectively, and Γ^0_X represents the number of equivalent sites corresponding to isomorphic substitutions (all expressed in sites m^{-2}). To simplify notation, we write pH = $-\log_{10}[H^+]$, while $[Na^+] = C_f$ denotes the salinity of the pore water solution. The resolution of equations equations A3 to A5 yields

807 $$\Gamma_{\mathrm{SH}}^{0}=\frac{\Gamma_{\mathrm{S}}^{0}-\Gamma_{\mathrm{X}}^{0}}{1+\frac{K_{\mathrm{H}}}{10^{-\mathrm{pH}}}\left(1+C_{f}K_{\mathrm{Na}}\right)}, \tag{A6}$$

808 $$\Gamma_{\mathrm{S}^{-}}^{0}=\frac{(\Gamma_{\mathrm{S}}^{0}-\Gamma_{\mathrm{X}}^{0})K_{\mathrm{H}}/10^{-\mathrm{pH}}}{1+\frac{K_{\mathrm{H}}}{10^{-\mathrm{pH}}}\left(1+C_{f}K_{\mathrm{Na}}\right)}, \tag{A7}$$

809 and

810 $$\Gamma_{\mathrm{SNa}}^{0}=\frac{(\Gamma_{\mathrm{S}}^{0}-\Gamma_{\mathrm{X}}^{0})C_{f}K_{\mathrm{Na}}K_{\mathrm{H}}/10^{-\mathrm{pH}}}{1+\frac{K_{\mathrm{H}}}{10^{-\mathrm{pH}}}\left(1+C_{f}K_{\mathrm{Na}}\right)}. \tag{A8}$$

811 All the charged sites that are not compensated in the Stern layer need to be compensated in
812 the diffuse layer. Therefore, the fraction of counterions in the Stern layer is defined by the
813 equations

814 $$f=\frac{\Gamma_{\mathrm{SNa}}^{0}}{\Gamma_{\mathrm{SNa}}^{0}+\Gamma_{\mathrm{S}^{-}}^{0}+\Gamma_{\mathrm{X}}^{0}}, \tag{A9}$$

815 and

816 $$f=f_{M}\left\{\frac{C_{f}K_{\mathrm{Na}}}{f_{M}(1+C_{f}K_{\mathrm{Na}})+(1-f_{M})\left[1+C_{f}K_{\mathrm{Na}}+\frac{10^{-\mathrm{pH}}}{K_{H}}\right]}\right\}, \tag{A10}$$

817 where f_M designates the highest value of f reached at high salinities, i.e.

818 $$f_{M}=\lim_{C_{f}>>1/K_{\mathrm{Na}}} f=1-\frac{\Gamma_{\mathrm{X}}^{0}}{\Gamma_{S}^{0}}. \tag{A11}$$

819 The value of f_M is approximately 0.99 for kaolinite, 0.90 for illite, and 0.85 for smectite. At
820 high pH values one has

821 $$f\approx f_{M}\left(\frac{C_{f}K_{\mathrm{Na}}}{1+C_{f}K_{\mathrm{Na}}}\right). \tag{A12}$$

822 Therefore, an increase of salinity is responsible for an increase of the partition coefficient, *f*,
823 which in turn is responsible for an increase of the magnitude of the quadrature conductivity
824 (see Revil, 2012).

825

Tables

Table 1. Properties of the two core samples. Porosity is non-kerogen matrix porosity. The reported density is bulk density (grain density is estimated at 2650 kg m^{-3}). Reference depth: Kelly bushing.

Sample	Depth (m)	ϕ	Density (kg m^{-3})	TOC (wt%)	Hydrogen Index	Maturation
Bakken A	2630	0.028	1,990	20.1	584	II
Bakken B	3098	0.032	2,220	12.1	436	III

Table 2. In phase σ' and quadrature conductivity σ" at different salinities ("I" stands for in-plane measurements while "T" stands for transverse measurements with respect to bedding plane).

	0.5 mM		0.05 M		0.5 M	
	in-phase	quadrature	in-phase	quadrature	in-phase	quadrature
Bakken A-I	7.82E-03	2.91E-05	1.01E-02	3.46E-05	1.54E-02	6.59E-05
Bakken A T	8.87E-04	4.65E-06	1.17E-03	5.52E-06	1.96E-03	4.03E-06
Bakken B-I	3.33E-04	6.29E-06	1.53E-03	2.06E-05	3.15E-03	3.21E-05
Bakken A-T	4.73E-05	9.23E-07	1.53E-04	2.72E-06	9.22E-04	4.05E-06

Table 3. Formation factor, F, surface conductivity, σ_S, porosity exponent, m, and tortuosity, τ ("I" stands for in-plane measurements while "T" stands for transverse measurements with respect to bedding plane). The tortuosity in a given direction is determined by the product of the formation factor times porosity.

Sample	F(I)	F(T)	σ_S (I, ×10^{-4} S/m)	σ_S (T, ×10^{-4} S/m)	m(I)	m(T)	τ(I)	τ(T)
Bakken A	543±100	3770±530	84±7	9.6±0.8	1.76	2.30	15.2	106
Bakken B	406±130	4350±30	3.2±0.8	0.43±0.03	1.75	2.43	13.0	139

Figures

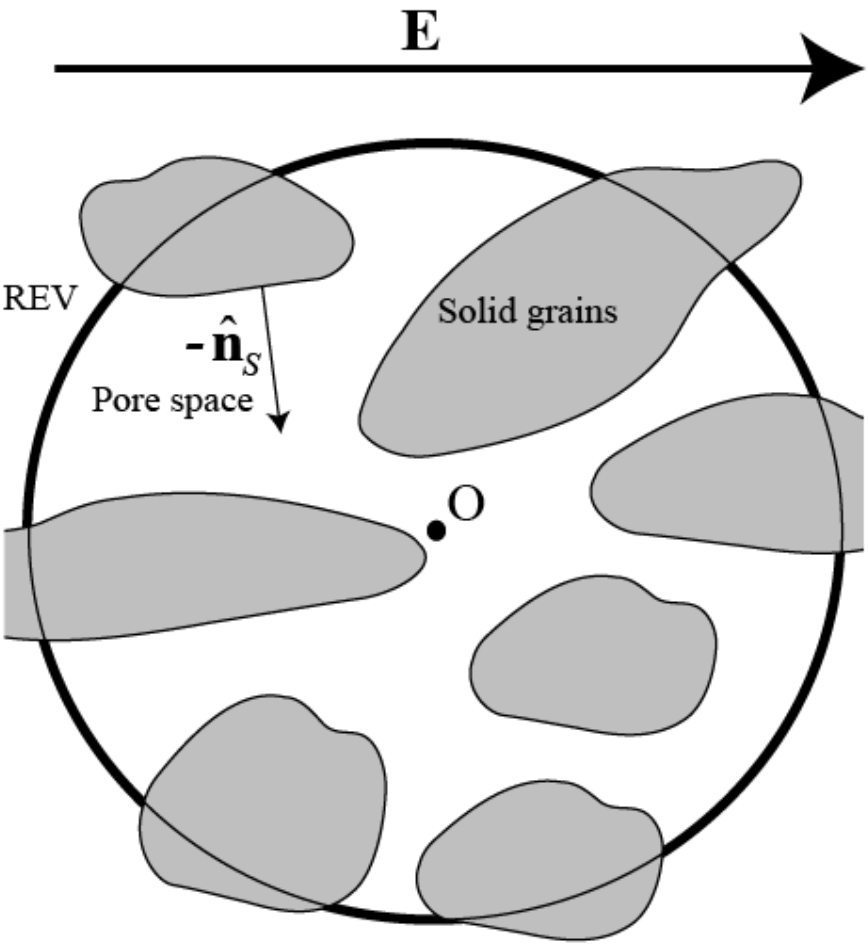

Figure 1. Description of the Representative Elementary Volume (REV) centered at point O. Vector $\hat{\mathbf{n}}_s$ denotes the unit vector locally normal to the grains, **E** denotes the macroscopic electrical field applied to the REV. The local electric field is written as **e** in the main text and, in absence of electrical double layer, it is locally tangential to grain surfaces.

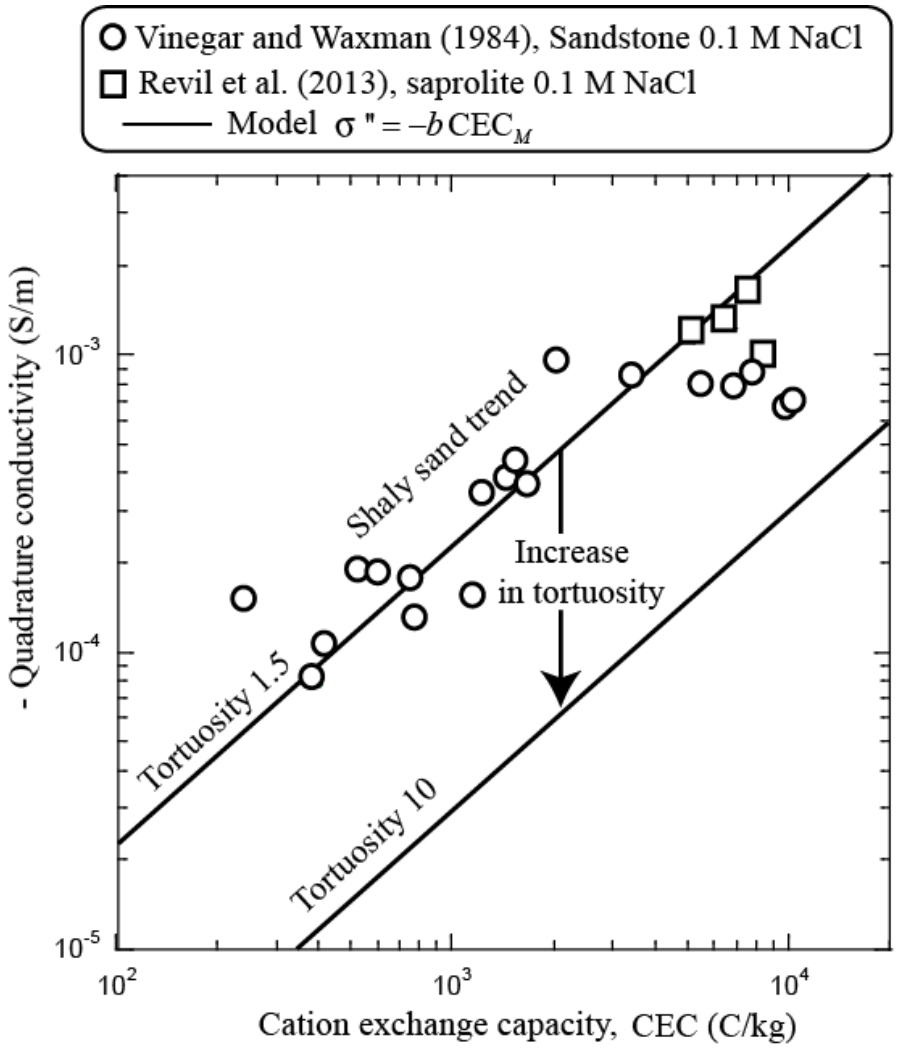

Figure 2. Linear relationship between quadrature conductivity and cation exchange capacity of clayey materials assuming fully saturated conditions (NaCl solution), equal salinity (0.1 M), same temperature, same frequency (approximately 10 Hz), and same pH range (5-7). The solid line was calculated for a tortuosity of 1.5. Higher tortuosities would generate lines parallel to the one shown but would predict smaller quadrature conductivity amplitudes for the same values of CEC and salinity.

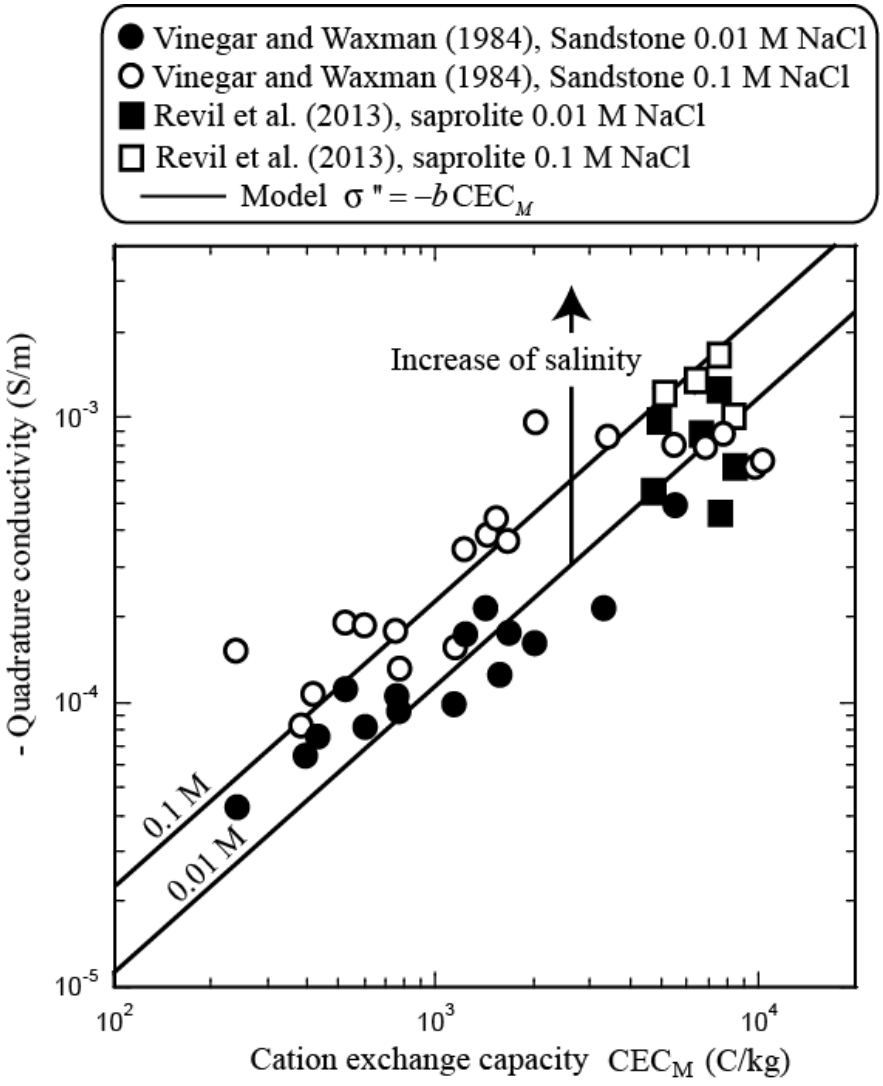

Figure 3. Influence of the salinity on the magnitude of quadrature conductivity. The increase of salinity is responsible for an increase of the magnitude of quadrature conductivity. In our model, this effect is related to the effect of salinity on the partition coefficient, *f*, of counterions in the Stern layer.

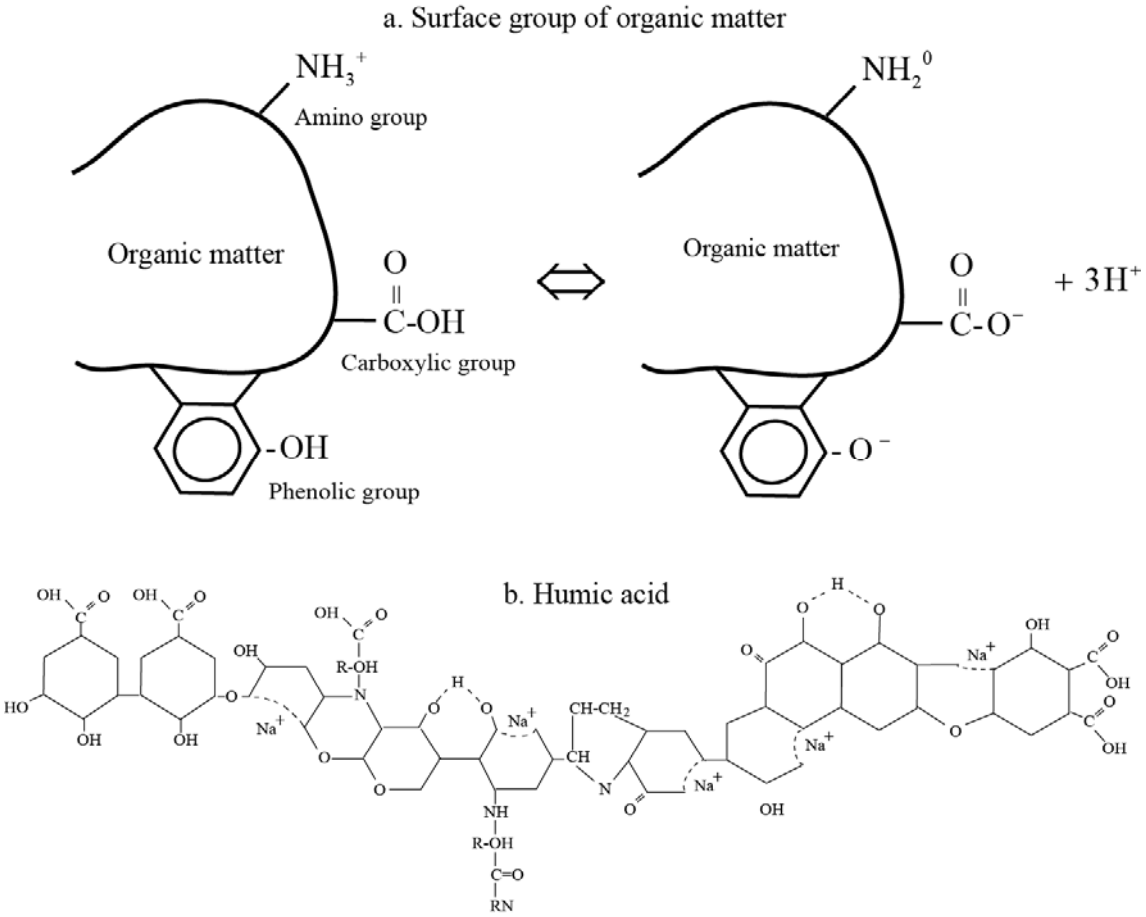

873
874

875 **Figure 4.** Surface sites of organic substances such as humic acids. **a.** The surface of organic
876 matter is generally negative at neutral pH values and is characterized by very high values of
877 specific surface area and cation exchange capacity. Surface charge can be positive below pH
878 2. In addition to a pH-dependent charge on the surface of these macromolecules, there is a
879 permanent electric charge associated with isomorphic substitutions. **b.** Example of humic
880 acid (Leonardite) showing different types of surface sites. Note that CEC also increases with
881 oxidation of such organic molecules (modified from
882 http://www.phelpstek.com/portfolio/samples/humic_acid.html).

883
884

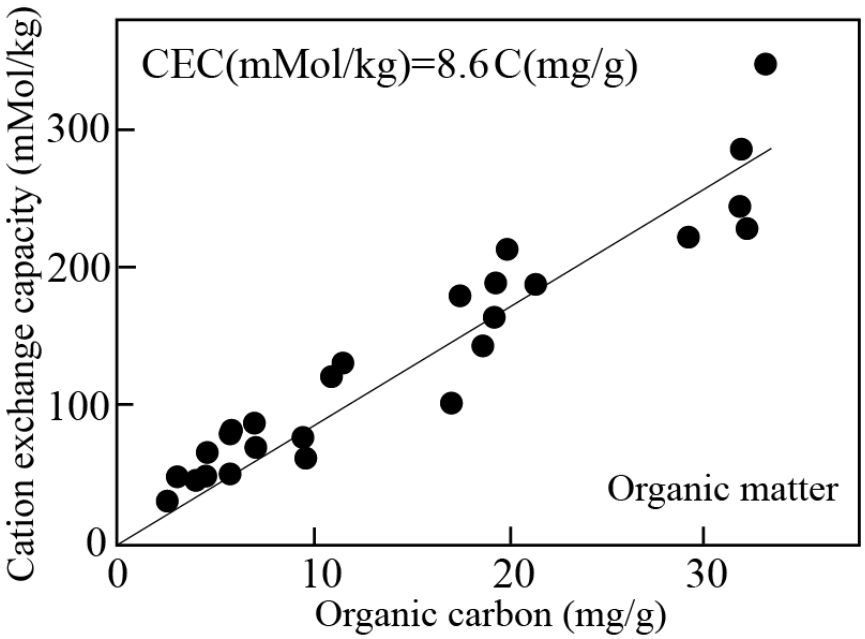

Figure 5. Correlation between cation exchange capacity (CEC) of organic matter and amount of organic carbon (weight concentration, experimental data from Liang et al., 2006).

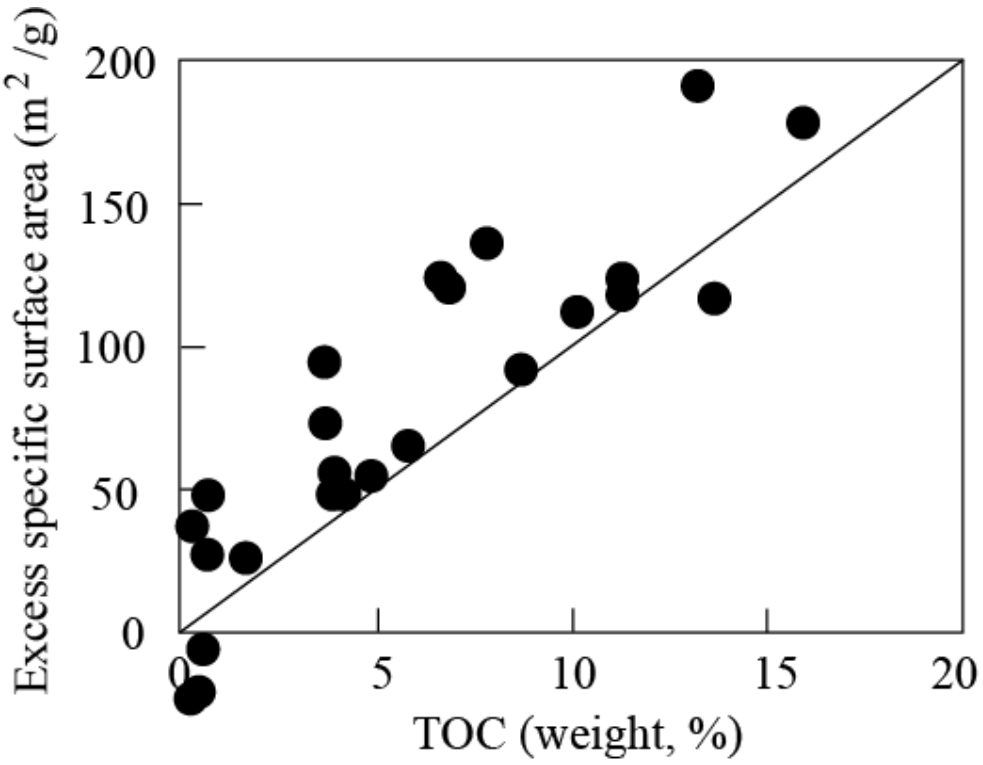

Figure 6. Relationship between excess specific surface area (clay contribution removed) and total organic content (weight%) for kerogen-rich oil shales. Data from Derkowski and Bristow (2012) for the Woodford formation.

902

903

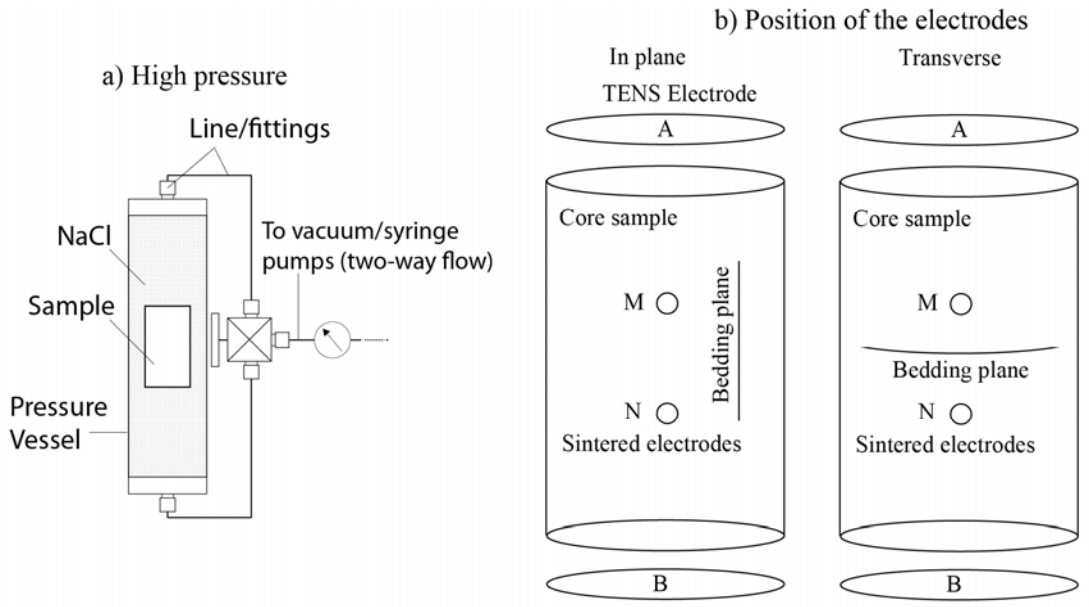

904

905

906

907 **Figure 7.** Cell and geometry of measurement acquisition for transverse and in-plane electrical
908 conductivity measurements with respect to bedding plane. **a.** Sketch of the cell. **b.** Geometry
909 of the electrodes. A and B denote current electrodes while M and N denote voltage
910 electrodes. The geometric factor was computed as $k = A/L$, where L is the distance between
911 the M and N electrodes (1/3 of the height of the sample) and A is the cross sectional area of
912 the cylindrical core sample. The current electrodes are coupled to the sample with a
913 conductive electrolytic gel-adhesive (designed for use on human skin in nerve stimulation
914 therpy applications), while the potential electrodes are coupled to the sample through a
915 conductive electrolyte gel. The current electrodes can be removed and reused in repeat
916 acquisitions ; here depticted as detached from the sample to illustrate the size and shape,
917 correspnding to the end faces of the sample. The sample surface (except at the position of the
918 electrodes) is covered with quick dry nail polish, which prevents desaturation and is a good
919 insulator.

920

921

922

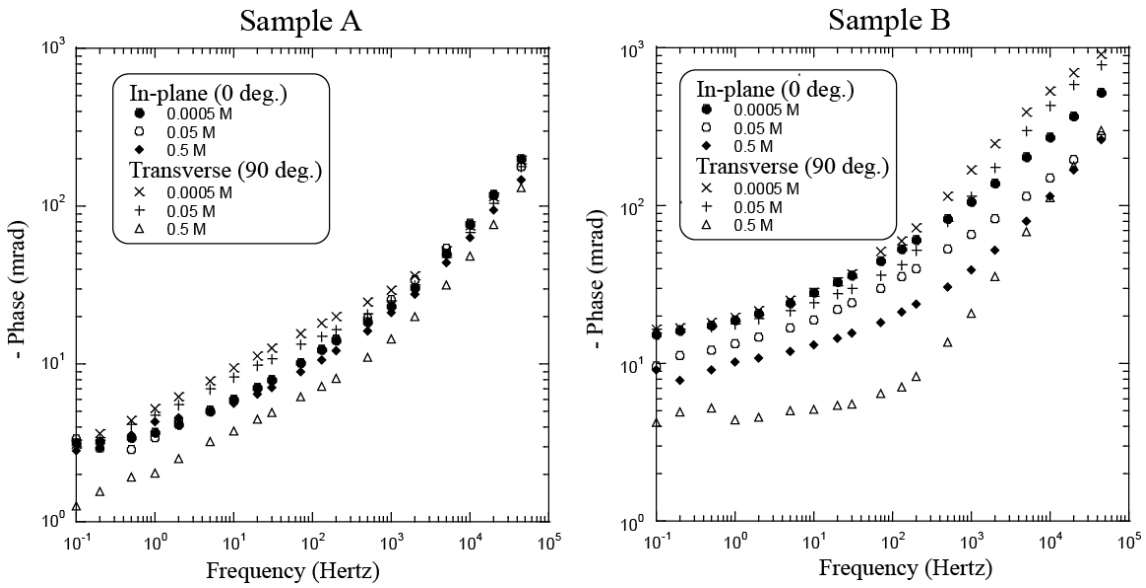

923

924

925 **Figure 8.** Measured phases for Samples A and B. Note the continuous increase of the
926 magnitude of the phase with the frequency. The high frequency response is likely due to
927 Maxwell Wagner polarization.

928

929

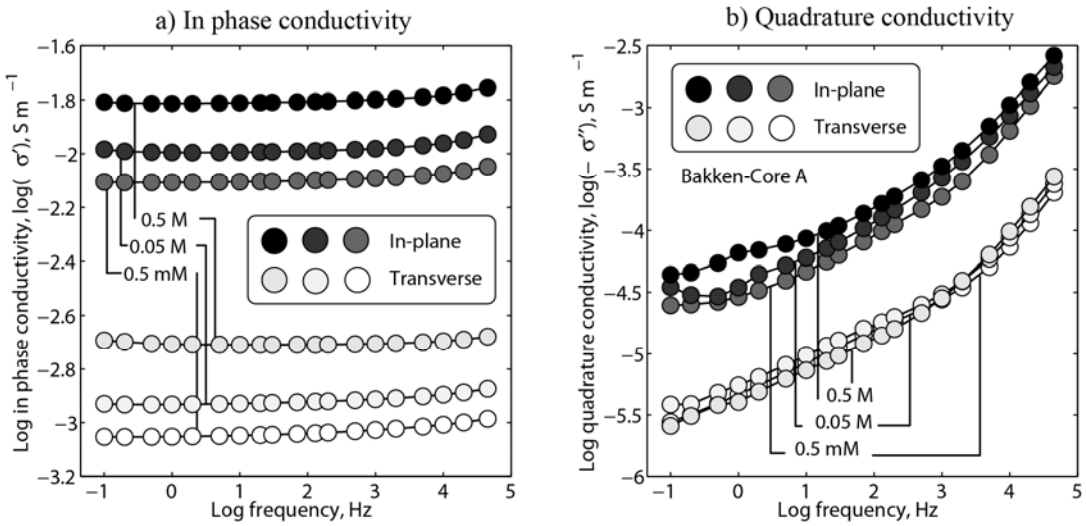

Figure 9. Complex conductivity spectra for Bakken core Sample A. **a.** In-phase electrical conductivity versus frequency at three salinities (0.5, 0.05, and 0.005 M NaCl). **b.** quadrature electrical conductivity versus frequency at three salinities (0.5, 0.05, and 0.005 M NaCl).

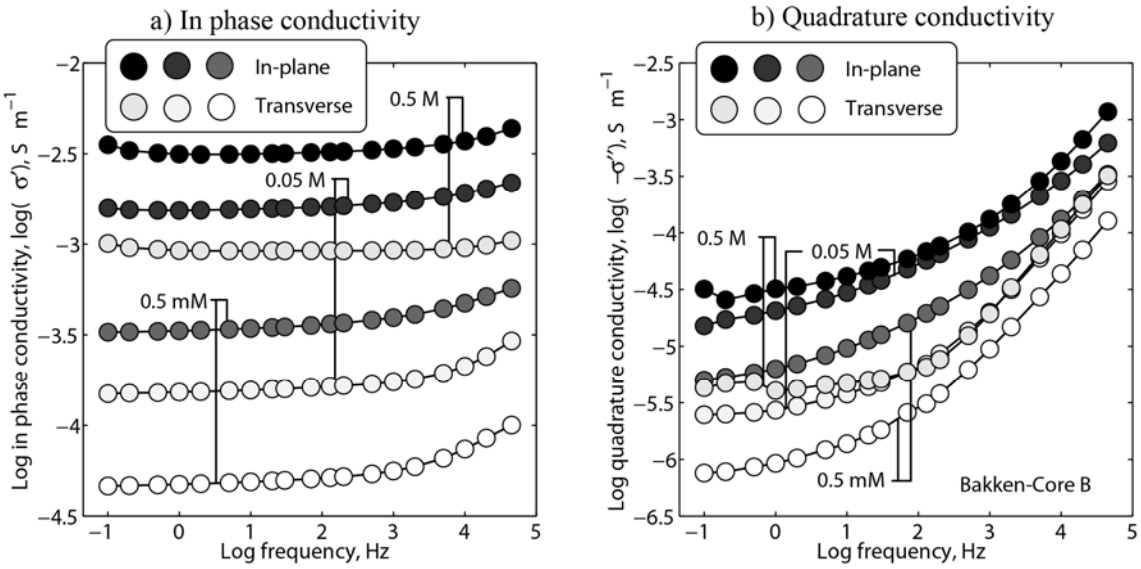

Figure 10. Complex electrical conductivity spectra of Bakken core Sample B. **a.** In-phase electrical conductivity versus frequency at three salinities (0.5, 0.05, and 0.005 M NaCl). **b.** quadrature electrical conductivity versus frequency at three salinities (0.5, 0.05, and 0.005 M NaCl).

954

955

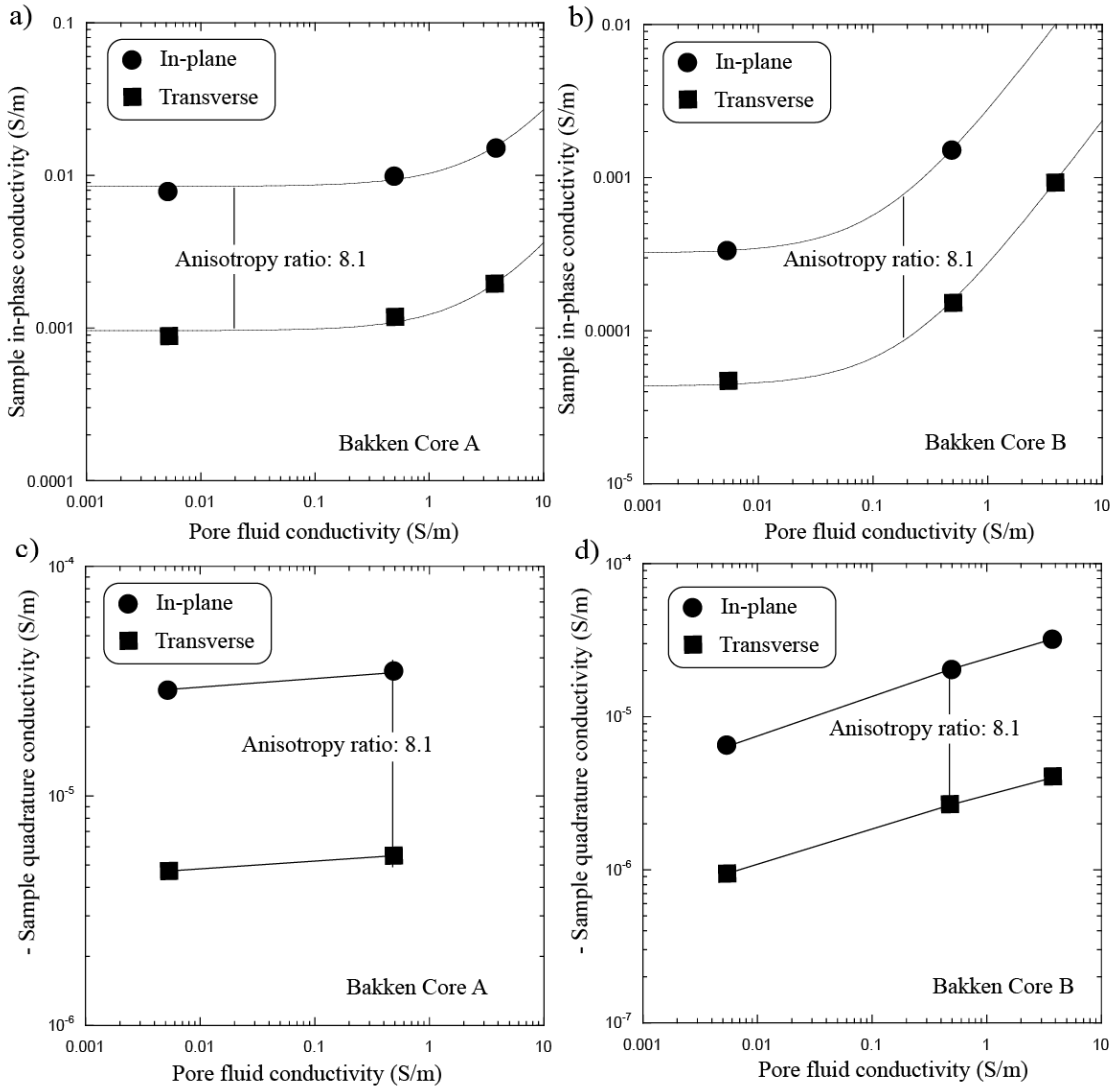

956

957 **Figure 11.** In-phase and quadrature electrical conductivities for core samples A and B at 1
958 Hertz. **a.** In-phase electrical conductivity, Sample A. Lines identify the model fit (equation 5
959 at saturation). **b.** In-phase conductivity, Sample B. For the two upper graphs, the lines
960 identify the model fit. Formation factors and surface conductivities are reported in Table 3. **c.**
961 Quadrature electrical conductivity, Sample A (the points at the highest salinity are not shown
962 because of their uncertainties). The vertical line serves as guide. **d.** Quadrature conductivity,
963 Sample B. For the two lower graphs, the lines serve as guides. Anisotropy ratio is defined as
964 the ratio of the highest to the lowest eigenvalues of the tensor; it exhibits a mean of 8.1±3.1
965 ($N = 12$).

966

967

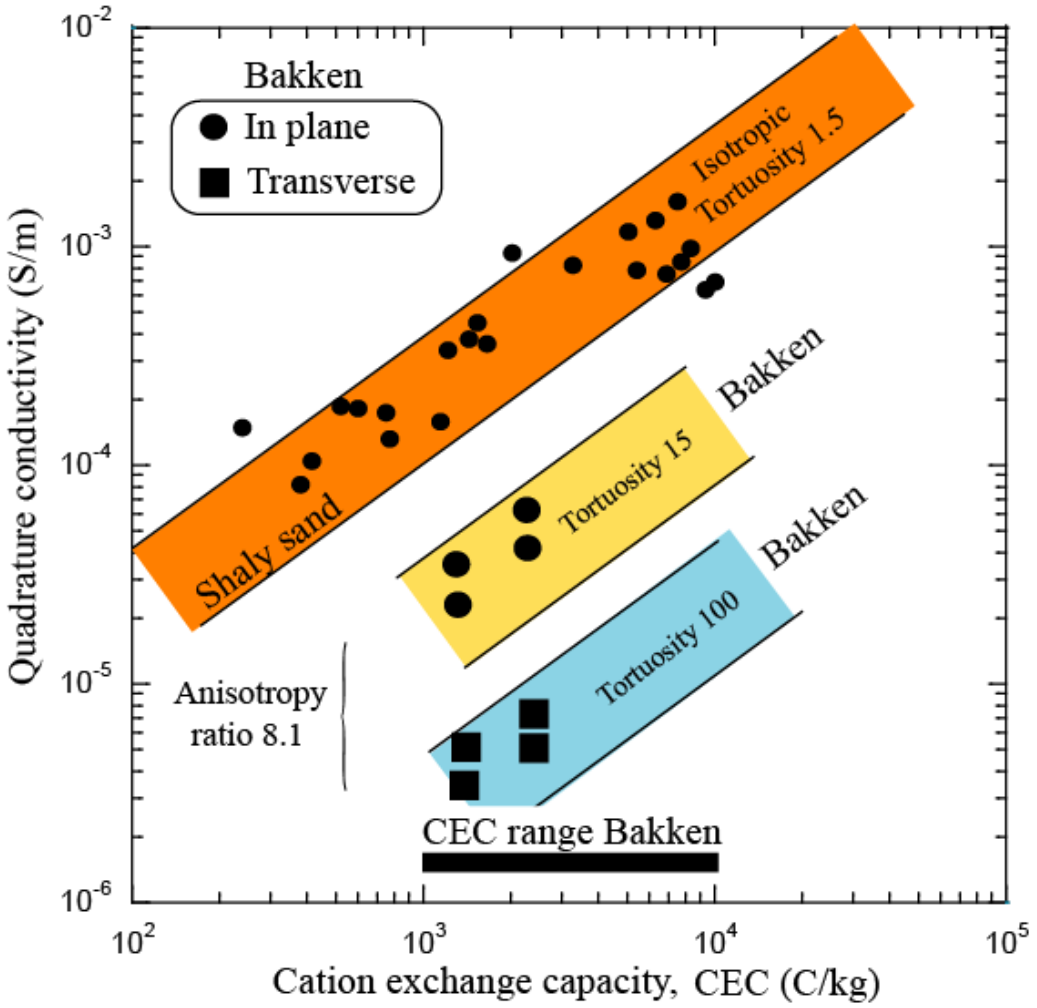

968

969

970 **Figure 12.** Influence of anisotropy and tortuosity upon quadrature conductivity (1 Hertz).
971 The high tortuosities found in Bakken rocks are responsible for a decrease of quadrature
972 conductivity at a given salinity and CEC. For Bakken rock samples, data are consistent with a
973 tortuosity value of 15 in the bedding plane and over 100 in the transverse direction.

974

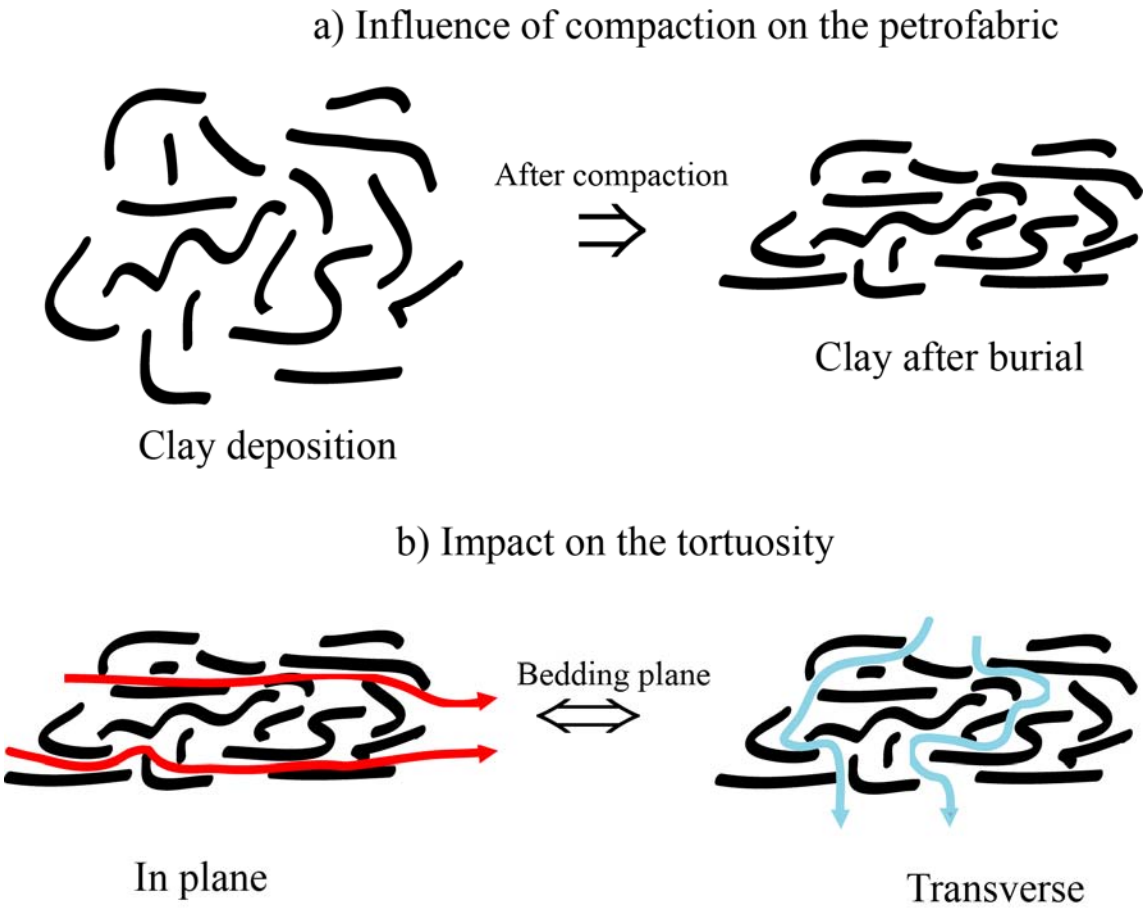

Figure 13. Influence of burial on both petrofabric and tortuosity tensor. **a.** Differential compaction is responsible for the formation of petrofabric in clayey materials (clay particles are shown in black). Depositional facies and burial are typically responsible for the formation of TI (transversely isotropic) media. **b.** In TI media, the in-plane tortuosity is expected to be much smaller than the tortuosity in the direction transverse to bedding plane.

984

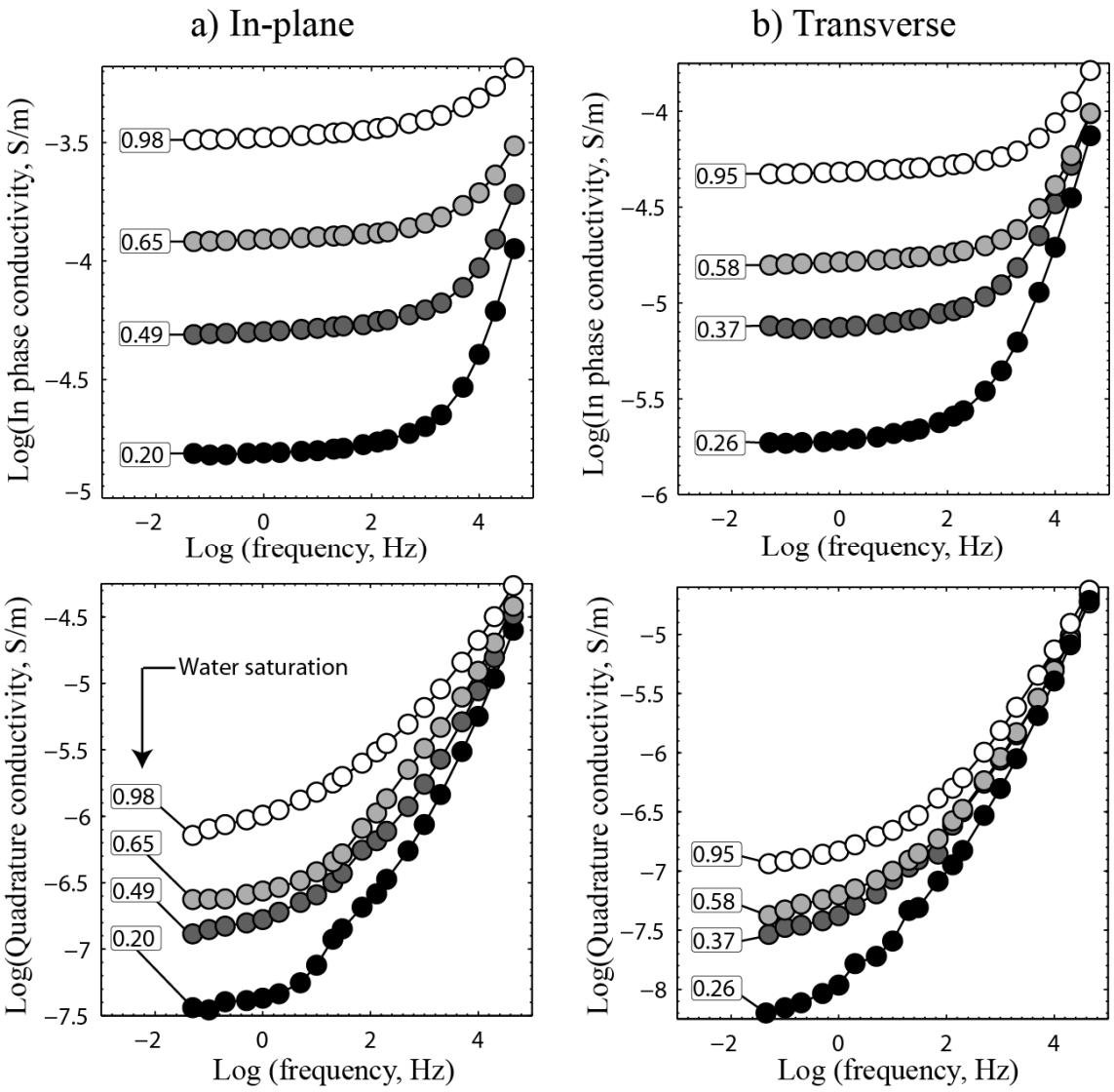

985

986

987 **Figure 14.** Influence of saturation upon in phase and quadrature conductivities of Sample B.
988 **a.** In-plane measurements for in-phase and quadrature conductivities. **b.** Transverse
989 measurements for in-phase and quadrature conductivities. Note that a change in saturation
990 affects the magnitude of the in-phase and quadrature conductivities, not the anisotropy ratio.
991 This result is consistent with our assumption to consider that *n* and *p* do not depend too much
992 on the direction.

993

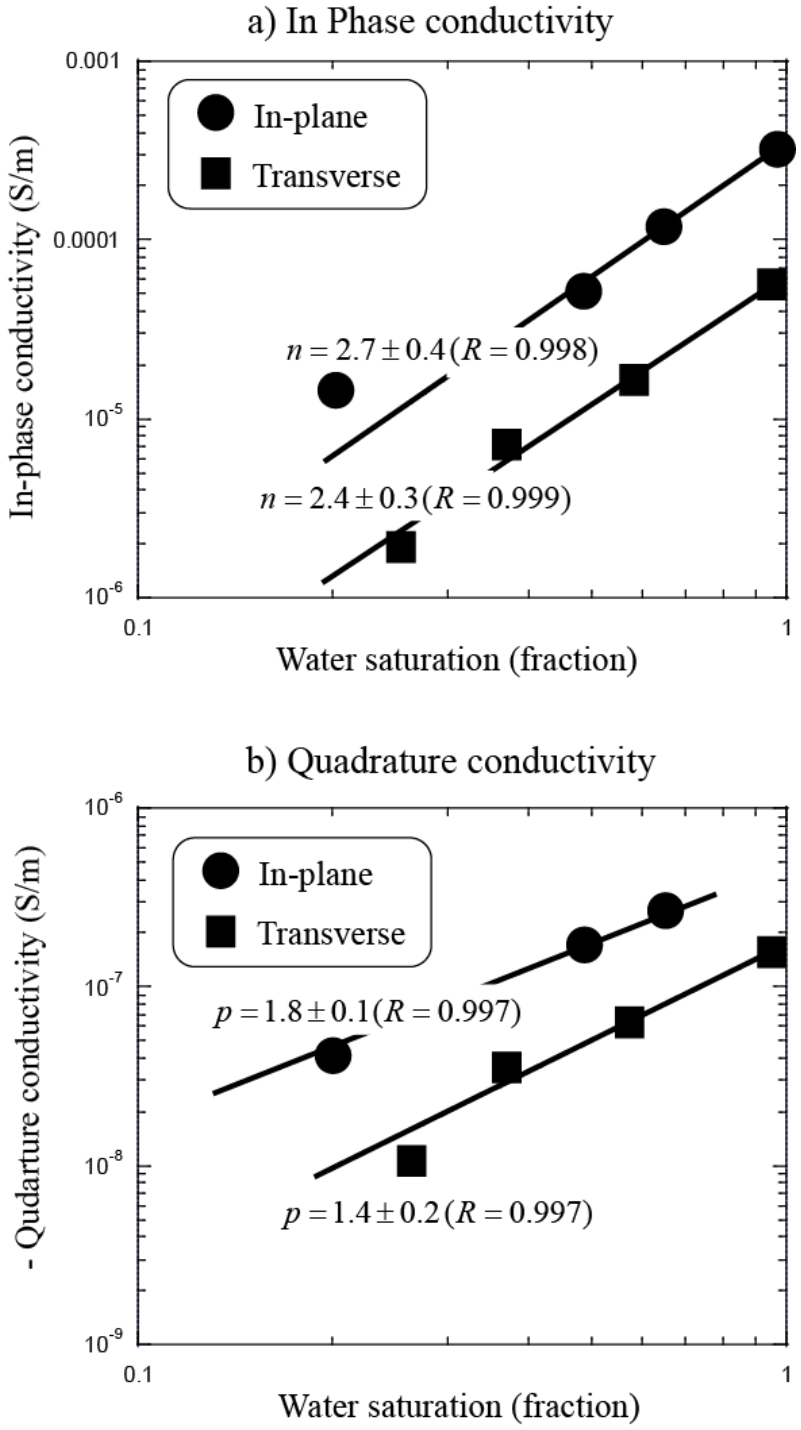

994

995

996 **Figure 15.** Influence of the saturation on the in-phase and quadrature conductivity of Sample
997 B at 1 Hz. **a.** In-phase conductivities (in-plane and transverse measurements). **b.** Quadrature
998 conductivities (in-plane and transverse measurements).

999

1000

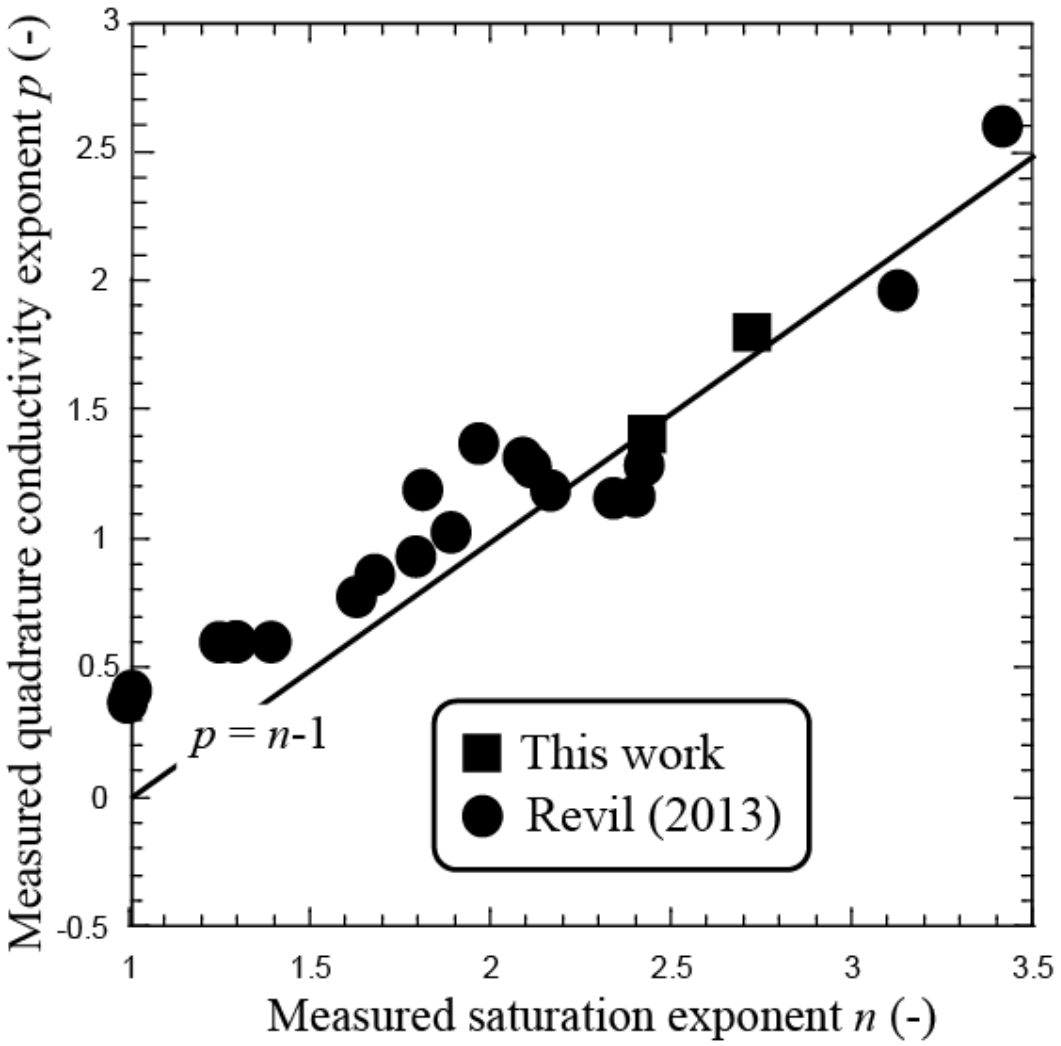

1001

1002

1003 **Figure 16.** Relationship between the p-exponent used to describe the saturation dependence
1004 of the quadrature conductivity and the n-exponent (saturation exponent) used to describe the
1005 saturation dependence of the in-phase conductivity when surface conductivity is negligible.
1006 The plain line corresponds to the relationship developed in Revil (2013), which is consistent
1007 with the prediction of the model of Vinegar and Waxman (1984).

1008